Neurovascular coupling conversely modulates emotion

Jiayu Ruan[1,2,3,4], Xinghua Quan[2,3,4], Yiyi Zhang[2,3,4], Huiqi Xie[2,3,4], Dongdong Zhang[2,3,4], Wentao Wang[2,3,4], Bingrui Zhao[2,3,4], Danping Lu[2,3,4], Jie-Min Jia[2,3,4*]

Affiliations

[1] College of Life Sciences, Zhejiang University, Hangzhou, Zhejiang, China.

[2] Westlake Laboratory of Life Sciences and Biomedicine, Hangzhou, China.

[3] Key Laboratory of Growth Regulation and Translational Research of Zhejiang Province, School of Life Sciences, Westlake University, Hangzhou, China.

[4] Laboratory of Neurovascular Biology, Institute of Basic Medical Sciences, Westlake Institute for Advanced Study, Hangzhou, China.

*Correspondence: jiajiemin@westlake.edu.cn

Summary

Emotion induces changes in regional cerebral blood flow (rCBF), a manifestation of neurovascular coupling (NVC). However, whether rCBF changes during NVC might, in turn, influence emotion is unclear. Here, by establishing arteriolar-optogenetic control of rCBF in free-moving mice, we demonstrate rCBF changes themselves induce emotional changes, and NVC actively modulates emotion. NVC deficiency impairs emotional flexibility, leading to contextually inappropriate emotional rigidity. Conversely, enhancing NVC counteracts this rigidity. To categorize inappropriate responses, we developed a predictive platform based on neural-activity patterns of the basolateral amygdala (BLA) in the mice exposed to a range of contexts. This platform revealed that NVC deficiency leads to BLA activations in a bipolar form, whereby predicting context-dependent hyper-reactivity and hypo-reactivity. Notably, this prediction was verified by actual physiological and behavioral responses. Mechanistically, neuronal mechanosensory receptor Piezo2 is essential for NVC-modulated emotion flexibility. Our findings establish NVC as an allostatic program for shaping emotion flexibility.

Introduction

Emotion changes over time, a key indicator of emotion flexibility.[1] Such flexibility involves the regulatory ability to adapt and respond to emotional experiences in a contextually appropriate manner.[2] Emotion regulation is of crucial significance for mental health and well-being.[3-5] Impairment in emotional flexibility can lead to emotion rigidity, which is one of the dimensions of emotion dysregulation and has recently been highlighted as a key contributor to psychiatric conditions.[2,6] Emotion rigidity manifests in two primary ways: restricted emotion ranges (reduced emodiversity) and context-inappropriate emotional responses.[2,7] Understanding the underlying molecular and cellular mechanisms of emotional flexibility and rigidity holds critical implications for elucidating basic biological explanations for resilience in the face of potential psychological trauma.[8,9]

Neuroimaging techniques, such as functional magnetic resonance imaging (fMRI), are instrumental not only in detecting emotion dysregulation but also in shedding light on the underlying neural mechanisms.[10,11] For instance, they have shown that hyperactivity or hypoactivity in the basolateral amygdala (BLA) can contribute to psychiatric conditions associated with emotion rigidity.[6,12] These neural activities are reflected indirectly through hemodynamic changes during neurovascular coupling (NVC), which forms the physiological basis for functional brain imaging.[13,14] Consequently, changes in

rCBF during NVC are often regarded as passive indicators.[15] Whether and how they might actively regulate neural circuit functions is unclear *in vivo*.

Alternatively, despite over a century of research, the definitive functions of NVC remain elusive.[16,17] This study seeks to explore this open question. Recent proposals suggest NVC's involvement in modulating cognition and neuropathologies[14,16,18] but the definitive role of local NVC in the BLA in influencing emotion flexibility and rigidity is poorly understood. To investigate this, two critical requirements must be met: first, achieving BLA-specific control of NVC in freely moving animals; second, selectively blocking the communication between neural and vascular systems without directly disrupting either system. Thus far, to our knowledge, no experimental paradigm meets these criteria, underscoring the urgent need to advance our understanding of NVC's functional roles.

Arteriolar smooth muscle cells (aSMCs) are a critical component in the neurovascular unit (NVU), effectively governing NVC,[19,20] and its contractility can be successfully controlled by optogenetics on the surface of the cortical cortex of head-fixed mice.[21,22] These reports have promised the feasibility of stimulation of aSMC-covered arterioles in the BLA of free-moving mice by combining with the currently well-developed fiber photometry technique. Moreover, such photometry can simultaneously record hemodynamics in deep-brain regions following intravenous injection of fluorescent dye.[23] This paradigm would allow simultaneous control and monitoring of rCBF during

NVC in freely behaving mice, meeting the requirements to address the central question of this study.

In parallel, independent mouse models are necessary to ascertain the consistency of the effects derived from the aforementioned optical control of NVC. For instance, a mouse model based on gene perturbations is essential. The genetic model should precisely block neurovascular communication, avoiding directly interrupting neural circuits and vascular integrity. However, because conventional pharmacology and null knockout models lack necessary cell-type specificity or directly interrupt neural circuitry,[24-27] meeting these requirements has seemed challenging. Although recently developed cell-type-specific NVC-deficient model may be able to address the central question,[28,29] their effects on modulating emotion have yet to be explored. More critically, these perturbations are global and cannot achieve brain-region-specific NVC manipulations, thus introducing ambiguity.

Here, we established the paradigm for simultaneous monitoring and optical controlling NVC in the BLA of free-moving mice. This paradigm, together with three more fundamentally distinct NVC-deficient models, all commonly indicate NVC deficiency impairs emotion flexibility. They exhibited one hallmark of emotion rigidity (context-inappropriate emotional hyperactivity or hyporeactivity, a bipolar-like manifestation). But they did not display the other hallmark (reduction of emodiversity). Notably, enhancing NVC helped mice gain resilience to emotion rigidity development following chronic stress.

Mechanistically, NVC deficiency caused hyperactivity or hypoactivity of BLA neurons in a context-dependent manner, reminisced with similar neuropathologies in the BLA of patients with psychiatric disorders.[6,12] Furthermore, vasomechanics during NVC seemed to be critical. Overall, this study further clarified the relationship between NVC and emotion, deepening our understanding of their reciprocal interactions and suggesting new insights into how to counteract the progression of emotion rigidity and intervene in emotional dysregulation.

Results

Developing an assay to simultaneously record the BLA's rCBF, control it, and monitor emotion-representing behaviors.

If rCBF changes have active roles, artificial manipulation of rCBF should be able to actively change mouse emotion status, even in the innocuous context of the home cage. To explore this, we first established an assay that integrated measurement and manipulation of BLA's rCBF in free-moving mice, alongside setting appropriate behavioral emotion indexes (EIs) from a range of potential EIs (Figure 1A).

We began this study with defecation behavior for the following two reasons. First, numerous studies in human research have established a relationship between emotion change and defecation behavior.[30] Second, in

animal studies, the defecation behavior has long been used as one of the EIs to reflect emotional changes induced by stress.[31-33]

Our findings further supported these conclusions by showing that BLA activity was required for defecation behavior induced by acute tube stress (Figure 1B-1C). Such stress induced every single mouse to defecate with no exception (saline group in Figure 1C right). The BLA inactivation by chemogenetics stopped three out of ten mice's defecation and reduced average fecal production (Figure 1B and 1C). We additionally found that the regular open field test (OFT) with minor stress intensity also induced defecation behavior, similarly requiring BLA's activity (Figure 1D). These results indicated that defecation behavior is an effective emotion representing index, shortened as EI_Defecation here, which was associated with BLA activity.

Moreover, we found that EI_Defecation exhibited a spatial preference similar to the frequently reported EI of time spent in the center area of the OFT, shortened as EI_Time-in-center (Figure 1E and 1F). Additionally, EI_Defecation showed a stronger preference for the peripheral area (Figure 1F). Thus, we decided to use EI_Defecation as the primary EI, combined with other EIs, for subsequent investigations.

After settling down the primary EI, we embarked on rCBF recording and manipulations as designed in Figure 1A. First, we successfully recorded the BLA's rCBF using fiber photometry recording of fluorescent signals in blood

plasma following venous injection of Rhodamine B (Figure 1G). We detected the increasing signals along multiple injections of higher doses, demonstrating effective recording of rCBF (Figure 1G-H. See Methods).

We next effectively suppressed rCBF in the BLA where arteriolar cells expressed light-sensitive channelrhodopsin2 (ChR2) in *SMA-creER:Ai32* mice (Figure 1A, 1I and Figure S1A). The specificity of this Cre-driver line to aSMCs was validated previously (Figure S1B).[19] After exploring a series of protocols, we finally identified one that can reliably and repeatedly suppress rCBF (Figure 1J shown in red line. See Methods). Once the light was on, rCBF became ~3% instantly lower than baseline; it immediately returned to baseline once the light was off (Figure 1J and 1K). These results indicated that we can reversibly control rCBF in the BLA. All these data thus demonstrated a comprehensive assay of measuring the BLA activity-associated behavioral EIs while simultaneously and artificially changing rCBF in the BLA.

Optogenetic reduction of the BLA's rCBF likely de novo implants emotion

Next, we performed arteriolar optogenetics in the home cages, a context with minimal external stress. We particularly chose a stable period to perform arteriole optogenetics (pointed by arrows in Figure 1L). Within the 15 minutes of light-On, the total amount of cerebral blood supply to the BLA was profoundly reduced in *SMACreER:Ai32* mice compared to that of the ChR2 negative group (ChR2^{-}, *SMACreER:Ai47* mice) that received all the same

handlings (Figure 1M and 1N).

To assess the EI_Defecation, all the previously produced feces in the home cage were first removed before a total of 45 minutes observation period (Figure 1M above). We defined the defecation rate as the percentage of mice that produce at least one fecal pellet during a specified observation period. Within this 45-minute observation period, ChR2^{-} mice only exhibited a defecation rate of 63.3% (9 out of 14 mice, Figure 1O left). In contrast, arteriole optogenetics induced every single *SMA-creER:Ai32* mouse to defecate with no exception, namely, a 100% defecation rate (Figure 1O middle), comparable to the results of the tube stress assay (Figure 1O right).

Notably, ChR2^{+} mice produced 1.14 fecal particles on average in 15 minutes, which was 3.7 times greater than that of ChR2^{-} mice, achieving levels not previously observed in the home cage environment (Figure 1P). Unequivocally, this acute, distal stimulation in the BLA avoided any direct stimulations on the local gastrointestinal tract that promotes bowel movement. Thus, these calculations of EI_Defecation suggested that the artificial changes in the BLA's rCBF under the context of home cage *de novo* implant emotion represented by EI_Defecation.

This conclusion was further consolidated by the finding that artificial changes in rCBF caused a robust increase in the BLA's neural activity (Figure 1Q and 1R). This result echoed the previous conclusion that the EI_Defecation can reflect BLA activity-associated emotion changes (Figure 1B-1D).

Altogether, these findings demonstrated a cause-effect relationship between rCBF change and emotion change.

NVC deficiency caused by arteriolar optogenetics promotes more rapid initiation of defecation, a sign of hyper-reactivity.

Although OFT is known to increase the BLA's neural activity represented by c-Fos expression level,[34] whether OFT can induce NVC, showing rCBF increase in the BLA, has not been directly determined. The deep-brain optical fiber photometry revealed rCBF increases once mice entered the open field box, indicating that NVC occurred in the BLA (Figure 1S-T).

Optical suppression of such NVC in *SMA-creER:Ai32* mice resulted in a hyperreactive-like response, as evidenced by a higher defecation rate, a trend of producing more feces (Figure 1U-1W). In contrast, the total running distance and EI_Time-in-center remained unchanged (Figure 1X and 1Y). Notably, NVC deficiency caused profoundly shortened defecation latency (Figure 1W), which was defined as the time from a mouse's introduction to a new environment of OFT until the first fecal pellet is produced. The finding of faster latency indicated that artificial NVC deficiency caused a more rapid initiation of defecation, suggesting a hyper-reactive-like status. Altogether, these data indicated that artificial suppression of NVC can induce a context-inappropriate emotional response, a sign of impairment of emotional flexibility.

Distinct models of NVC deficiency commonly eventuated a hyper-reactivity to OFT with mild stress

Recognizing that arteriolar optogenetics may inadvertently introduce unknown side effects, we established three more types of NVC-deficient models. Each type is based on different foundational principles (cell-type-specific genetic knockout (cKO), local siRNA, and high-fat diet). If they all commonly induce hyper-reactivity-like behavior, it would further strengthen the conclusion that NVC deficiency impairs emotional flexibility.

Regarding the first cKO-type model, based on the previous finding of neural–arteriolar smooth muscle cell junction (NsMJ, Figure 2A),[19] we established four genetic tools (*SMA-creER:Grin1*$^{f/f}$, *SMA-creER:Grin2d*$^{f/f}$, *SMA-creER:Grin1*$^{f/f}$*:Grin2d*$^{f/f}$, and *Pdgfrβ-creER:Grin2d*$^{f/f}$), which are maximally devoid of the direct disturbances of neural circuit or vascular integrity.[19] Meanwhile, to have comparators, three more NVC-deficient lines were generated by directly targeting neurons (*Emx1-cre:Ptgs2*$^{f/f}$) and vascular contractile proteins (*Pdgfrβ-creER:Acta2*$^{f/f}$). *SMA-creER:Ptgs2*$^{f/f}$ was used as a potential negative control. *Emx1-cre* was used to target nearly all excitatory neurons;[35] *Ptgs2* encodes prostaglandin-endoperoxide synthase 2, also known as cyclooxygenase-2 (COX2), producing potent vasodilators.[24] *Pdgfrβ-creER* was used to target all mural cells that encompass SMCs and capillary pericytes;[19] *Acta2* encodes smooth muscle alpha-actin (α-SMA), a contractile protein critical for arteriolar contractility.[20]

Our prior work targeted the NMDAR core subunit GluN1 in aSMCs,[19] and in this study, we identified *Grin2d* (Gene name of GluN2D) as the only detectable non-core NMDAR subunit in aSMCs (Figure 2B and 2C). First, RNAscope confirmed *Grin2d* presence in aSMCs (Figure 2D), and the probe's specificity was first verified in cerebellum tissues (Figure S2A and S2B).[36] Next, after the anit-GluN2D antibody was strictly verified (Figure S2C),[37] we found that GluN2D protein was present in aSMCs of littermates but absent in those of *SMA-creER:Grin2d*$^{f/f}$ mice (Figure 2E-2G). Neither neural disruptions (Figure 2H) nor changes in contractile proteins (α-SMA and smoothelin) were observed (Figure S2D and S2E). Also, we found GluN2D undetectable in peripheral SMCs, which minimized systemic side effect concerns (Figure S3). In addition, we also excluded tamoxifen administration's possible side effects on NVC (Figure S4). All these examinations suggested that we neither directly altered neural circuits nor caused any functional defects in myogenic tone.

Similarly, the effectiveness of *Ptgs2* and *Acta2* perturbation was carefully verified (Figure S5). Functionally, we evaluated all these seven genetic cKO lines by combining laser spectral contrast imaging (LSCI) measurements with the traditional whisker stimulation paradigm.[38] Except for *SMA-creER:Ptgs2*$^{f/f}$ mice, the other six genetic cKO lines all effectively suppress NVC in the barrel cortex (Figure S6).

We then chose *SMA-creER:Grin2d*$^{f/f}$ as the exemplary line to further determine whether BLA's NVC can also be suppressed (Figure 2I and 2J). The

basal levels of rCBF during the home cage between the two genotypes were comparable (Figure 2I inserted panel). These observations suggested that the genetic cKO lines may only compromise the amplitude of NVC without affecting basal CBF supply to the BLA. We thus inferred that all these genetic cKO lines may globally affect NVC, beyond BLA and barrel cortex.

Surprisingly, the EI_Defecation increased in whichever NVC-deficit lines, indicating that they responded more intensely than typical to OFT (Figure 2K). First, qualitative analysis revealed that all defecation rates were nearly twice as high in all NVC deficient lines than in control mice (87.5%-100% vs. 50%-64.29%, percentiles in Figure 2K). In addition, the urination rate was generally consistent with the defecation rate (Figure S7). Second, consistently, quantitative analysis revealed that all NVC-deficient lines produced approximately three times more fecal particles than controls on average (Figure 2K). Collectively, these findings revealed a general negative correlation between the NVC and EI_Defecation: the decreased NVC, the increased EI_Defecation (Figure 2L).

Among these lines, the EI_Defecation observed in *Emx1-crePtgs2*$^{f/f}$ and *Pdgfrb-creER:Acta2*$^{f/f}$ lines even approached levels akin to those induced by the tube stress assay (Figure 2K). We characterized this increased defecation as a type of hyper-reactivity. Altogether, these genetic cKO lines of NVC deficiency manifested a hyper-reactivity as observed optical suppression of NVC in *SMACreER:Ai32* mice (Figure 1U-1W).

We took *SMA-creER:Grin2d*$^{f/f}$ line as an exemplary line for further detailed examinations. Similar to *SMA-creER:Ai32* mice (Figure 1W), we found a profoundly shorter defecation latency (Figure 2M). Some *SMA-creER:Grin2d*$^{f/f}$ individuals immediately defecated once entering the box, which was never observed in controls. In the 15-minute OFT test, *SMA-creER:Grin2d*$^{f/f}$ mice exhibited the strongest EI_Defecation response in the first 5 minutes, producing nearly 12 times more feces than controls (Figure 2N, also see vertical dashed lines in Figure 2I). This response decreased over the next two 5-minute periods, with fecal output 3.5 times higher in the second period and 3.0 times higher in the third period (Figure 2N). Again, there was no difference in the total running distance and EI_Time-in-center (Figure S8), consistent with the results from the optically stimulated ChR2^{+} mice (Figure 1X and 1Y).

Intriguingly, there was a neat, negative correlation between the sizes of the OFT and the EI_Defecation of mice with normal NVC (Figure 2O and 2P). Littermate control mice showed a gradual increase in EI_Defecation in OFT boxes with decreasing floor areas of 40*40 cm², 35*35 cm², and 10*10 cm² (Figure 2O and 2P). In great contrast, NVC-deficient mice exhibited an abrupt increase in EI_Defecation rather than a gradual style. This finding indicated the ability of mice to modulate the intensity of emotional responses in a context-dependent manner. The abrupt plateau again indicated that NVC deficiency led to context-inappropriate emotional responses, a status of

impaired emotional flexibility. (Figure 2P right).

Local NVC deficiency modeled by siRNA targeting aSMC-specific protein

In addition to the arteriolar optogenetics, we achieved another local model of NVC deficiency. It is unavoidable to directly interrupt neurons if we choose siRNA targeting GluN2D or GluN1, because they are also expressed in neurons.[39] Therefore, we switched to determine whether there are molecular targets that are not only GluN2D binding proteins but also exclusively expressed in aSMC. We identified one protein called caldesmon[40] functionally interacting with GluN2D to mediate NVC (Figure 2Q and 2R). We applied the proteomic analysis for the protein complex that was pulled down by using the anti-GluN2D antibody to incubate with the primary aSMC cell lysates. The KEGG analysis of this complex revealed an enriched pathway of vascular smooth muscle contraction pathway (Figure 2Q).

After their interaction was further verified by Western blot and immunoprecipitation (Figure 2R), we designed and evaluated the effective siRNAs targeting *Cald* (gene name of caldesmon. Figure 2S). Cisterna magna injection of *Cald*-siRNAs indeed effectively suppressed NVC in the barrel cortex following whisker stimulation (Figure 2T and Figure S9A). Thus, we applied intracranial stereotactic injection of a strictly controlled amount of siRNA (1 nM/100 nl) to achieve BLA-specific vascular perturbation so that even the nearby regions were not affected (Figure 2U and 2V). For example,

ventromedial nucleus of the hypothalamus was not affected (Figure S9B-S9D). More importantly, knocking down *Cald* in the BLA did not functionally affect the NVC in the barrel cortex (Figure 2T). This would allow BLA-specific NVC manipulation, which the Cre-lox system-mediated genetic model cannot achieve.

Notably, local NVC deficiency in the BLA, despite intact NVC in the rest of the brain regions, resulted in a 100% defecation rate, three times higher than that of scrambled siRNA-injected mice (Figure 2K). Furthermore, a combination of the local model and the genetic cKO model failed to increase EI_Defecation further, suggesting that caldesmon acted in the same pathway with GluN2D (Figure S9E and S9F).

Collectively, these results confirmed that both models of BLA-specific NVC deficiency (optogenetic and siRNA-mediated), together with the global cell-type-specific genetic cKO model, commonly induced emotional hyper-reactivity (Figures 1U-1W and Figure 2K).

Obese mice induced by a high-fat diet show inappropriately intense reactions to mild stress when blood-brain barrier (BBB) is still intact

We next extended to the obesity model induced by the high-fat diet (HFD), which is known to induce NVC deficiency (Figure S10A and 10B).[41] Although HFD-induced obesity involves intricate, multifaceted, and nonspecific effects, it can serve as a fundamentally distinct way to interrupt NVC compared to the

above approaches. Importantly, obese humans with body mass index (BMI) > 30 are believed to have NVC deficiency.[42]

Notably, HFD-treated mice exhibited high EI_Defecation despite that they consumed less amount of food than controls and produced fewer fecal pellets in their home cage (Figure 2K, 2K inserted panel, and Figure S10C-S10E). Even though they only received the mild stress resulting from OFT, their EI_Defecation was even approaching the degree of tube stress with a 100% defecation rate and an average above four fecal pellets (Figure 2K). These data strongly demonstrated that the increased EI_Defecation was not due to increased food intake but a context-dependent emotional response.

Moreover, we excluded the possibility that this emotional change is attributed to BBB leakage (Figure S10F and S10G), despite BBB leakage being frequently observed in HFD treatments and typically associated with emotional changes.[18,43] This exclusion was based on the observations that both NVC and emotion changes occurred in the fourth week of HFD when BBB appeared intact (Figure 2K, Figure S10F, and 10G). This timeline aligned with the commonly reported BBB leakage in the eighth week.[43]

In summary, we established four types of fundamentally distinct models of NVC deficiency (BLA-targeting arteriole optogenetics, global genetic cKOs, local siRNA, and HFD). In general, the overall physiological features, including gastrointestinal (GI) system and BBB integrities, were unchanged, except for body weight and fat content in the HFD group (Figure S10C and S10D). These

indicated such emotional change was not likely due to systemic physiological side effects across these models (Figure S11).

Even though these four types of models might have entrained their own side effects, their common effects on incurring hyper-reactivity to mild stress, showing impaired emotional flexibility. This common effect suggested a potentially universal link between NVC and emotional regulation. NVC may serve as a necessary allostatic program for the brain to avoid generating an overwhelmed emotional response to as mild stress.

NVC deficiency results in BLA hyperactivation, which is responsible for emotional hyper-reactivity.

Next, we asked about the molecular and cellular mechanisms underpinning NVC-deficiency-induced hyper-reactivity. We hypothesized that such hyper-reactivity was due to BLA hyperactivation in NVC-deficient mice because of the following two findings. First, local rCBF changes sufficiently activated BLA neurons (Figure 1M, 1N, 1Q, and 1R). Second, BLA neural activity was required for stress-induced defecation behavior (Figure 1B-1D). In *wild-type* rodents, BLA's c-Fos is known to increase upon OFT,[34] so we predicted more c-Fos increase in NVC-deficient mice than in littermates. We examined two models, *SMA-creER:Grin2d*$^{f/f}$ and local *Cald* siRNA. Indeed, both models exhibited hyperactivated BLA upon OFT (Figure 3A and 3B).

To further consolidate the above findings, we employed real-time

recording of rCBF and neural Ca^{2+} in the BLA. We transduced the BLA excitatory neurons with *AAV-CaMKIIa-Gcamp8s*, which expressed a protein probe to detect Ca^{2+} changes. We observed elevated neuronal Ca^{2+} signals in the littermates with healthy NVC (Figure 3C and 3D), consistent with the c-Fos results (Figure 3A and 3B).[34] Excitingly, we indeed observed higher Ca^{2+} signals in the NVC-deficient mice, directly demonstrating hyperactivation, aligning with c-Fos results (Figure 3A-3D). Altogether, these findings demonstrated that the lower the capacity of NVC, the higher BLA activity.

Lastly, we chemogenetically inactivated the BLA of NVC-deficient mice (*SMA-creER:Grin2d*$^{f/f}$). Indeed, deprivation of such hyperactivation stopped the hyper-reactivity represented by the EI_Defecation (Figure 3E). This provided a neural mechanism explaining how NVC deficiency led to hyper-reactive emotional responses.

Neuronal Piezo2 perceives NVC deficits and is partially responsible for the hyper-reactivity

During NVC, arterioles dilate and exert mechanical forces on surrounding neurons. Removing NMDAR from aSMCs reduces arteriolar dilation [19]and thus may reduce mechanical forces. If neurons possess mechanosensitive proteins that detect these forces, depleting these proteins could mimic NVC deficits in *wild-type* mice. This is because neurons would lose their ability to sense arteriolar dilation, even though the dilation occurs normally.

As transcriptomics research profiled,[44] BLA neurons express the mechanosensory protein Piezo2. We knocked it down via virus injection into the BLA of *wild-type* mice (Figure 3F and Figure S12). Notably, Piezo2-knockdown (KD) partially recapitulated the key features of NVC deficient *SMA-creER:Grin2d*$^{f/f}$ mice: hyperactivated of BLA (Figure 3G and 3H) and partial increase in EI_Defecation (Figure 3I). These findings indicated that Piezo2-KD mice presented slight hyper-reactivity upon OFT. This suggested that Piezo2 in BLA excitatory neurons is partially responsible for NVC-dependent emotion regulation.

Create a predictive platform to categorize the exaggerated emotional reponses mismatched with the actual stress level.

To classify the extent of exaggerated emotional responses caused by NVC deficiency, we developed a predictive platform that can define a spectrum of stress levels. We created a library of BLA sections from seven groups of mice; each group underwent distinct contexts that may differently activate BLA (Figure 4A top, and Figure S13). This library encompassed a broad spectrum of stress levels, ranging from nearly no stress (home cage) to strong stress (predator-like threats. Figure 4A top panel). The latter were mimicked by traditional looming assay and the newly established virtual reality of eagle diving (VR_{eagle}). By using this library, we calculated a prediction index (PI) based on the degree of similarity of the BLA neural activation patterns across

different contexts (Figure 4A top). The similarity calculation integrated two dimensions of the BLA neural activity: anatomical distribution and their intensity of c-Fos signals (Figure S13. See Methods).

An image analysis specialist performed unbiased classification for this library by using this PI (See Methods). This specialist then revealed four stress levels denoted as levels 0 to 3 (Figure 4A top). As expected, the home-cage context generated the lowest stress (Level_0), and the predator-like-threat context generated the highest stress (Level_3) (Figure 4A top). OFT is known to cause mild stress and was positioned at Level_1, just right next to the home-cage context. Moreover, the two contexts of OFT_40*40 and OFT_35*35, known to be very similar to each other, were unbiasedly classified together, self-reflecting the PI reliability (Figure 4A top).

To further test the PI's discriminative capacity, we generated a complex version of the OFT (c-OFT) that can generate stronger stress. We introduced a natural insecurity element associated with a bright-white floor. Prey C57/B6 mice are known to feel more stressed on white floors and more secure on black floors.[45] We divided a chamber with a metal fence, with a white-floored left and black-floored right sides (Figure S14A). Each mouse was placed on the white side, allowing it to see but not cross into the darker side. The PI ranked the context of c-OFT at Level_2, demonstrating its discriminative ability because it distinguished the c-OFT one level higher than regular OFT and one level lower than predator threats (Figure 4A top).

Interestingly, the tube-stress context was positioned at Level_2, lower than predator threats. This could be possible because we did not force mice but waited until they spontaneously entered the tube, and we only restrained them for 15 minutes, substantially shorter than the typical ranges of up to 3 hours of restraint time often reported.[46] This appropriate positioning of tube stress again demonstrated the reliability of the PI of the prediction platform.

Regarding the highest Level_3, we updated the looming system (Figure S14B) to the VR_{eagle} system (Figure S14C), which simulates an eagle-diving scenario through a video played in a ballroom, creating a more realistic environment. Their stress levels are theoretically the closest. Indeed, they were ranked together based on the PI (Figure 4A top). Altogether, the PI can appropriately rank the seven contexts in an order aligned with the known stress levels (Figure 4A top and Figure S13).

By establishing this predictive platform, we revealed a regularity in the relationship between stress levels and the patterns of BLA activity in mice with normal NVC (Figure 4A top panel). Profoundly, NVC deficiency disrupted this regularity, represented by the distorted c-Fos patterns shown in the exemplary genetic cKO line of *SMA-creER:Grin2d*$^{f/f}$ mice, which underwent the same seven contexts (Figure 4A bottom). Only the home-cage context remained unchanged between the two genotypes (Figure 4A bottom and Figure 4B), aligned with previous findings of comparable basal characterizations (Figure 2I inserted panel and Figure S11).

Once again, the PI was even able to reveal unbiasedly that the *Cald*-KD and *SMA-creER:Grin2d*$^{f/f}$ were the two most similar groups, which was exactly as expected since caldesmon was first identified as working on the same pathway with GluN2D (Figure 2Q, 2R, Figure S9E, and Figure S9F). Additionally, this indicated that despite locally or globally impaired NVC, they similarly hyper-activated the BLA neurons.

After the above validations, we proceeded to classify the mismatched stress levels that NVC-deficient mice were likely to 'feel'. In the prediction platform, the PI ranked "cKO_OFT_40" at Level_2 despite these mice experiencing actual stress of Level_1, indicating hyper-reactivity, aligning with observed behavioral responses (Figure 2K and Figure 4C). It appeared that when *SMA-creER:Grin2d*$^{f/f}$ mice entered a regular OFT, they hyper-reacted as if they had entered an environment with the stress level of c-OFT or tube stress. This prediction was consistent with previous actual EI_Defecation observations (Figure 2K). Similarly, the local *Cald* KD treated group also had consistency between our predictions and observed behaviors (Figure 2K and Figure 4D). Thus, our predictions and actual observations commonly showed that NVC-deficient mice hyper-responded to a mild context as if they encountered more intense stress.

Intriguingly, arteriole optogenetics prompted a dramatic jump in the stress levels by two levels: from the Level_0 to Level_2 (Figure 4E). Given that c-OFT and tube stress at Level_2 both induce complex and mixed emotions, it is

possible that we optically implanted a mixed artificial emotion into the free-behaving mice (Figure 1U-1Y).

Surprisingly, the PI predicted that *SMA-creER:Grin2d*$^{f/f}$ mice would hypo-respond to looming and VR_{eagle}, a stark and paradoxical contrast to the predicted and behaviorally validated hyper-reactivity to OFT (Figure 2K and 2L). Instead of the expected further increase in stress levels, the *SMA-creER:Grin2d*$^{f/f}$ mice showed a decrease, stepping down from Level_3 (red) to Level_2 (yellow) (Figures 4F, 4G, and S15A). This unexpected prediction required actual physiological and behavioral validations.

NVC deficiency led to hypo-reactivity to innate fear threats

The complete sequence of an innate fear response in prey includes five steps, integrating both cognitive and behavioral components.[47] Cognitively, it includes predator recognition (Step_1), threat assessment (Step_2), and decision-making on flight or alternative defenses (Step_3). Behaviorally, it involves executing the chosen action (Step_4), relaxing defense, and returning to a normal state once the threat diminishes (Step_5).[47] The last step matters for the survival of individuals and species in a wild world because premature relaxation may make them more susceptible to surprise attacks.[48]

Recognizing that a single EI_Defecation is insufficient to capture all these dynamics occurring in these five steps (Figure S15B), we similarly incorporated additional behavior-based EIs, such as changes in pupil size and

locomotion speed. While EI_Defecation remained a robust indicator of innate fear, it failed to differentiate between the two genotypes as in the OFT context (Figure S15B and 15C).

In the looming assay, mice would not receive looming stimulation until they reached a locomotion speed of 13-15 cm/s, with no difference in basal locomotion between the two genotypes (Figure 5A blue-shadow and Figure S16A). The looming consistently induced instant typical freezing behavior in both genotypes with speed reduced to 1-2 cm/s (freeze status) (Figure 5A flesh-shadow). This implied that NVC-deficient mice had a normal innate fear response from Step_1 to Step_4 (Figure 5A), which appeared contradictory to the prediction (Figure 4F).

We continued to determine the Step_5 of relaxing defensive status. We generated a heatmap that profiled locomotion speed dynamics until 21 seconds after threats because this time window would be long enough to cover the most reported full duration of defensive states in *wild-type* mice.[49,50] This heatmap revealed that NVC deficiency led to premature relaxation of defense (Figure 5B). We found a substantially shorter period required for returning to normal status (Figure 5B and 5C) as well as more rearing behaviors representing a more relaxed state (Figure 5D). This finding of Step_5 was consistent with the prediction (Figure 4F).

To assess the cognitive recognition of threats (Step_2), we upgraded the looming threat to the VR_{eagle} system, encompassing both visual and auditory

threats. We examined locomotion speed and pupil size, an involuntarily controlled EI.[49,51] We recorded these two EIs simultaneously from awake, head-fixed mice with semi-free moving on a floating ball (Figure S14C and Supplementary Video 1). The two baselines of locomotion and pupil size between the two genotypes were not different (Figure S16B and S16C).

Similarly, stimulation commenced only after the mice began moving. When exposed to a distant-sounding eagle screech recording, both genotypes displayed a similar transient decrease in locomotion speed without changes in pupil size (Figure 5E, dashed and solid lines). These observations suggest that the mice perceived the distant screech as a potential threat, yet not imminent enough to cause harm. This supports the notion that Step 2, threat assessment, was comparably executed by both genotypes.

Upon the eagle's dive following the screech, both genotypic mice exhibited fear responses, evidenced by a similar increase in pupil size and concurrent freezing behavior (arrows in Figure 5E and Figure S16D). This response marked a second decrease in locomotion speed, deeper and more prolonged than the initial reduction caused by the screech (Figure 5E). These observations confirm normal visual processing and threat recognition from Step 1 to Step 4.

Thus, we again investigated the last step of relaxing defense (Step_5). The maximum of two independent EIs (largest pupil size and slowest locomotion) took place almost at the same time point (Figure 5E, arrows). After

this time point, Step_5 began as pupil size started to decline, and locomotion speed started to rise. We observed that Step_5 had a fast initial phase. We defined this initial phase from the endpoint of the eagle's dive (brown line) to the time point when the two dashed and solid curves came across, indicated by magenta and blue vertical lines (Figure 5E). Profoundly, NVC deficiency led to a shorter initial phase of Step_5 (Figure 5E and 5F), indicating potential premature defense relaxation.

The two independent assays of looming and VR_{eagle} commonly revealed that mice with normal NVC took an average of 12 seconds to fully relax from a defensive state back to normal status (Figure 5G, blue dots). To our great surprise, these two assays indicated almost identical time reductions between the two genotypic mice (59.05% in looming and 59.61% in VR_{eagle}, Figure 5G). These data immediately suggested that NVC deficiency prompted premature relaxation by more than two times faster. This might be caused by lower BLA activation. Therefore, these actual physiological and behavioral evaluations validated the prediction of hypo-reactivity to predator-like threats (Figures 4G and 5A-5G).

To exclude the effect of predator-type dependency, we designed a paradigm–letting mice watch a video of an approaching cat, an independent type of predator (Cat_{video}, Figure 5H-5L, and Figure S14D). First, we recorded the behavioral responses of awake, head-fixed mice on a treadmill repeatedly stimulated by Cat_{video} with three trials (Figure 5H and Supplementary Video 2).

As expected, normal mice showed typical defensive behaviors such as retreat and tail rattling (Figure 5I-5L), demonstrating that Cat_{video} was an effective stimulus. Notably, most NVC-deficient mice exhibited no retreat behavior at all (Figure 5J and 5K). Even among the rest of the small subset of this group, the intensity of defensive behaviors was also remarkably reduced (Figure 5H, and 5J-5L). These behavioral characterizations suggest that the found hypo-defensiveness was not predator-type-dependent (Figure 5E-5L).

Altogether, these actual behavioral evaluations corroborated the prediction. This consensus between the predicted and observatory results showed that NVC was required for shaping contextually appropriate emotional responses–emotional flexibility–by preventing the bipolar form of hyper- and hypo-responsiveness.

NVC-deficient mice are predicted to hypo-react to real social stress, verified by actual behavioral evaluation.

In addition to the above virtual and designated threats, we challenged the prediction platform with a substantially more complex context, which is more dynamically interactive and real mouse-mouse social stress. We decided to generate social stress by cohabitation with selected socially aggressive CD1 mice in a fresh home cage (Figure 6A). In a single-time cohabitation for a brief 10 minutes, we observed an average of 20 seconds of fighting, accounting for only 4% of the total time (Figure 6B). This was substantially shorter than

reported, which may be due to using fresh home cages, new to both mice.[52] The home cage was separated into small and large subregions, but mice were still allowed to freely inter-entrance between them (Figure 6A).

In the prediction platform, the PI positioned control mice experienced this social stress at Level_1 (green), more intense than in a home cage but less than tube stress (Figure 6C). Intriguingly, this was different in *SMA-creER:Grin2d*$^{f/f}$ mice (Figure 6D). They were predicted as if they perceived a stress level of Level_0 (blue), like in a home cage. This predicted a hypo-responsiveness to real social stress, which was again subsequently validated by actual behavioral evaluations.

Due to fear, although both two genotypes exhibited a natural tendency to avoid staying in the same smaller subregion with CD1, *SMA-creER:Grin2d*$^{f/f}$ mice showed less avoidance to CD1 than littermate controls (50 sec vs 100 sec out of a total of 600 seconds, Figure 6E). More strikingly, 98% of control mice actively fled away from CD1 after fights, and so did only 37% of NVC-deficient mice (Figure 6F). Consistent with the mice flee rate, we normalized it to total fighting events. There were 37 and 19 fights between the 8 controls with CD1 and 10 NVC-deficient mice with CD1, respectively, among which CD1 actively triggered the most fights (Figure 6G). NVC-deficient mice exhibited a significantly smaller percentage of fleeing rate than controls (Figure 6G). The sniffing behaviors did not differ between the two genotypes, indicating comparable basal exploratory ability (Figure 6H).

The consensus between the predicted results (Figure 6C and 6D) and actual behavioral verifications (Figure 6E-6G) strongly supported the prediction platform as reliable and the conclusion that NVC can modulate emotional status.

NVC-enhancement resists emotion rigidity caused by chronic restraint stress

Chronic restraint stress (CRS) is known to impair NVC and lead to emotion rigidity, like anxiety- and depression-like status.[53,54] If NVC is truly capable of modulating emotion, NVC-enhancement should be able to influence the development of emotion dysregulation following CRS.

Next, we embarked on developing an NVC-enhancement model, as no such model currently exists to our knowledge. Given that disrupting a cation channel, such as the NMDA receptor (NMDAR), suppresses NVC (Figure 2I), [19] we hypothesized that disrupting an opposite anion channel might enhance NVC. Our experimental results confirmed this hypothesis (Figure 7).

Previous transcriptomic studies showed that perivascular mural cells express ligand-gating chloride channels, for instance, glycine receptor subunit b (GlyRβ, encoded by gene *Glrb*).[55] It seemed highly expressed in venular SMCs (vSMCs, Figure S17A).[55] We confirmed *Glrb* puncta and GlyRβ protein clusters with more frequency found in vSMCs than aSMCs (Figure 7A-7D). We conditionally knocked out *Glrb* specifically in mural cells using

Pdgfrβ-creER:Glrb$^{f/f}$ (Figure 7C, 7E, and 7F) and further identified GlyRβ colocalizing with gephyrin *in vitro* (Figure 7G), a scaffold protein often segregated in inhibitory postsynaptic sites,[56] suggesting that GlyRβ could be clustered on the postjunctional membrane of glycinergic-NsMJ. This speculation was further supported by the finding that frequent direct contact of neural axons onto venular SMCs by both confocal laser scanning microscope (Figure 7H) and electron microscope (Figure 7I).

Notably, the whisker stimulation assay revealed that *Pdgfrβ-creER:Glrb*$^{f/f}$ mice indeed enhanced NVC, approximately 37.25% higher than averaging from littermate controls (Figure 7J and 7K). Together, these data suggested that functional glycinergic-NsMJ suppressed physiological NVC, so removing it would lead to enhanced NVC.

We hypothesized that if *Pdgfrβ-creER:Glrb*$^{f/f}$ mice with NVC enhanced can counteract the NVC deficiency caused by *Grin2d-cKO,* they may also be able to counteract hyper-reactive behaviors. Indeed, double knockout mice not only resisted hemodynamic attenuation during NVC (Figure 7J and 7K) but also resisted the hyper-responsiveness by comparing the two groups of *Pdgfrβ-creER:Grin2d*$^{f/f}$ *single cKO mice* and *Pdgfrβ-creER:Grin2d*$^{f/f}$*:Glrb*$^{f/f}$ double cKO mice upon regular OFT (Figure 2K and Figure 7L). These observations led us to test further whether *Pdgfrβ-creER:Glrb*$^{f/f}$ is able to counteract emotion rigidity, such as depressive-like emotional distress caused by CRS. We applied CRS to *Pdgfrβ-creER:Glrb*$^{f/f}$ mice to test this hypothesis.

After the *wild-type* mice were forced to stay in the tube for 2 hours every day for 28 consecutive days, they showed higher anxiety-like status, reflected by a shorter period of staying in the open arm of the elevated maze (Figure 7M left). In addition, they produced stools with changed quality after CRS (Figure 7M right), confirming CRS induction was effective in this study.[30]

Notably, *Pdgfrb-creER:Glrb*$^{f/f}$ mice completely resisted the changes in defecation behaviors and the quality of stool (Figure 7N-7P). They appeared to be even as normal as sham mice never received CRS (Figure 7N-7P). Alternatively, the forced swimming test (FST) was believed to reflect the degree of desperation in depression-like mice according to their duration of immobilization in the water. More strikingly, FST revealed a complete resistance to the development of depression-like status (Figure 7Q). The constant movements of *Pdgfrb-creER:Glrb*$^{f/f}$ mice in water were unlikely due to the increased basal level of locomotion because they exhibited normal locomotion in the OFT (Figure S18). In contrast, *Pdgfrb-creER:Glrb*$^{f/f}$ mice exhibited the lightest body weight over the course of CRS (Figure S17B), suggesting that NVC-enhancement only partially resisted emotional distress.

CRS is also known to impair BBB, which has been frequently associated with later emotional distress.[18,46,57] An alternative possibility could be that *Pdgfrb-creER:Glrb*$^{f/f}$ mice may be through protecting BBB leakage to resist the effects of CRS. Because we restrained mice for a 4-week period shorter than reported[57] and also because we observed no IgG leakage in parenchyma, we

conclude that BBB seemed intact under the current experimental settings (Figure S17C and S17D).

All these data emphasized that NVC may be a future therapeutic target for psychiatric disorders that are associated with emotion rigidity. Taking all NVC manipulations through this study together, we assert that NVC is a built-in program to modulate emotion.

Discussion

This study identified modification of emotion as one of the functions of NVC, directly addressing the longstanding question regarding the definitive function of NVC.[16-18] Unexpectedly, NVC actively engaged in the central nervous system computation for programming innate fear emotional response, a defensive system that promotes survival (Figures 4-5). NVC actively shaped emotional flexibility (Figures 2, 4-5), a factor crucial for mental health and well-being. For example, in high-stress situations such as emergency response or combat, the ability to regulate emotions can significantly impact decision-making and survival.[58] These findings may provide an explanation for the evolutionary conservation of NVC across species, as appropriate emotion regulation can be a matter of life or death in the animal kingdom and, at times, in human society as well. More importantly, this study offers a fundamental perspective on emotion regulation programs, promising a new avenue of

intervention in psychopathological progression by enhancing NVC, thus complementing current strategies.

Neurovascular coupling––What next ?

Although enormous amounts of academic effects have been put into measuring human's rCBF and understanding NVC mechanisms by Mosso, Roy, and Sherrington since the late 19th century, [59,60] the NVC research has come to a new door—what next? By knocking on this door, this study provides an unexpected renewal for this topic using state-of-the-art technologies that combine arteriolar optogenetics, real-time recordings of rCBF and neural Ca^{2+} in the deep brain regions of free-moving animals, cell-type-specific gene perturbations, and local vascular siRNA.

By exploring the BLA-emotion axis as an exemplary case, we propose that NVC can reversely regulate brain functions. It merits further investigations of this concept beyond emotion regulation in other brain regions where NVC also occurs. For instance, robust NVC occurs in the anterior cingulate cortex (ACC) when the ACC is involved in many brain functions and disease conditions, such as the affection and cognitive aspects of pain and social exclusion,[61] the transitions between wakefulness and sleep and its relations with insomnia disorder,[62] and psychogenic erectile dysfunction (PED).[63,64] Then, whether NVC has regulatory roles in the pathophysiology of chronic pain, insomnia, and PED merits further investigation. This study opens the next door to the

NVC research field.

Defecation behavior is a robust and sensitive EI

The amygdala is known to project to Barrington directly, a defecation and urination center located in the brainstem of mice.[65,66] Therefore, we extrapolated that BLA may send emotion-related neural signals to Barrington's nucleus, resulting in defecation. Suppression of BLA neurons by chemogenetic inhibition suggested the functional relationship between BLA and defecation (Figure 1C and 1D).

All seven contexts in this study can readily cause robust defecation behavior compared to the home cage (Figure 2K, 2L, and Figure S15B), mirrored with robust increases in BLA's c-Fos while with diverse patterns (Figure 4A and Figure S15A). This diversity indicates that although different contexts engaged distinct neuron subgroups, they all can eventually converge to defecation behavior (Figure 2K). This may explain why the EI_Defecation is sensitive EI while with limited discriminative ability (Figure 2K and Figure S15B). This may also explain why defecation behavior can be commonly induced despite those opposite changes in rCBF following OFT and optical stimulation, resulting in distinct c-Fos patterns (Figure S15B).

We propose that the EI_Defecation can be used for fast and/or pilot screening readouts because it is an assessment with robustness, simplicity, and objectivity. The analysis of defecation locations in the OFT (Figure 1E and

1F) highlights the potency of using the EI_Defecation has been overlooked. We recommend a broader scope in the mood research field to include the EI_Defecation. For example, in depression research, recently, the two classic tests of tail suspension and forced swimming have recently been under heated debates.[67,68] The findings following chronic restrain stress in this study implicate that the EI_Defecation might be a robust, alternative evaluation of depressed status.

In addition, the EI_Defecation was prone to differentiate the impact of NVC under the contexts of mild stress but failed to do so under the contexts of strong stress (Figure S15B). However, this could be due to this study's limited diversity of contexts or due to the investigation scope of this study. Multiple physiological and behavioral emotion indexes (e.g. pupil size, freeze/flight) are necessary, depending on specific context and scientific questions.

Neurovascular calculations should be considered in the basic psychiatric study.

This study opens up a new field of how NVC actively participates and helps in fine calculations during neural computations, highlighting not merely at the synaptic level[69] but also at the neurovascular level. The neurovascular computation seemed intrinsically programmed to optimize the kinetics of a single cycle of fear response to predators, specifically determining the timing of the transition into a defensive state and the subsequent relaxation from that

state. This neurovascular calculation should be taken into account by the basic affective study of emotion flexibility.

This study emphasizes the critical role of bidirectional neurovascular communications in a functional entity. Such bidirectional communications may provide a unique biological insight into the next-generation algorithm development for artificial intelligence if future robots need to include multi-hierarchical modulatory modes of emotion designs.[70]

Neurovascular coupling (NVC) and vasculo-neuronal coupling (VNC) function in a loop manner that is interlinked

NVC could, conversely, immediately send various types of signals back to neurons when vasodilation is induced by neural activity. Among these signals, a mechanic signal attributed to vasodilation could be one of them. This backward vascular-neural talk is referred to as vasculo-neuronal coupling (NVC). [71-73] We believe that the neurons that cause NVC may or may not be the same group of neurons that perceive vasomechanics. If they are two separate groups, future work could focus on whether the two groups also communicate with each other. Thus, the NVC–VNC loop, sequentially programmed, eventually satisfies the bidirectional communications between the nervous and cerebrovascular systems.

NVC is generally thought to oversupply blood flow where needed.[16] How neurons sense and respond to vasodilation during NVC has emerged as a new

research field.[71,73] This study broke the NVC-VNC loop by blocking VNC part (Figure 3G-3I). Despite blocking VNC by knocking down neuronal Piezo2-KD in *wild-type* mice, a similar trend was found in EI_Defecation as if in NVC-deficient mice (Figure 2K and Figure 3I). This suggested that this loop functioned as an interlinked program. Future investigation is needed to determine the neuron subgroups that control vasodilation and sense vasodilation.

Enhancing NVC may provide a new intervention

To our knowledge, this study, for the first time, developed a genetic model that enhanced NVC: *Pdgfrβ-creER:Glrb*$^{f/f}$. This is likely achieved by blocking glycinergic NsMJ, meaning glycinergic axon innervating vessels. During NVC, there are believed to be negative and positive factors for regulating vasodiameter.[74] We extrapolate glycinergic NsMJ as a negative factor. In *Pdgfrβ-creER:Glrb*$^{f/f}$ mice, such a negative factor was removed, so the NVC was enhanced. Nevertheless, the detailed molecular mechanism underlying such potential negative regulation needs to be elucidated.

Previous work reported that glycinergic axon terminals can be observed both in BLA and involved in depression regulation.[75,76] Enhanced NVC in *Pdgfrβ-creER:Glrb*$^{f/f}$ mice may prevent hyper- or hypo-neural activations in the BLA so that it can completely counteract emotion rigidity caused by chronic stress. If the mural cell-specific virus is established, interruptions of GlyRβ will

have implications for developing new therapeutic approaches for psychiatric conditions.

In addition, the vascular-cell transcriptomic study revealed that GlyRβ transcripts are more expressed in mural cells of venules compared to capillary pericytes and aSMCs.[55] This study also opens a new avenue for studying the contribution of venules in brain functions.

In summary, this study is based on comprehensive models to expand our understanding of the relationship between NVC and emotional regulation, highlighting NVC actively participating in programming emotional flexibility. The study also agrees with a growing consensus that the function of NVC is far beyond the regulation of CBF and is involved in regulating cognition and emotion at different scales.

Acknowledgments

We thank Y. T. and X. H. for sharing *Nestin-cre* and *Emx1-cre* mice. We thank Y. Z. for sharing psychological knowledge to facilitate our understanding of data. We thank Y. N. for the KEGG map drawing. We thank Westlake University Laboratory Animal Resource Centre for guiding behaviour assays. We thank the Microscopy Core Facility of Westlake University for imaging guidance. We thank the Mass Spectrometry & Metabolomics Core Facility (MSMCF) of Westlake University for mass data collection. We thank the Flow

Cytometry Core Facility (FCCF) for cell sorting assistance. J.-M.J. acknowledges the support from Westlake Laboratory of Life Sciences and Biomedicine (Project No. 202309002), Westlake University startup funding, the Westlake Education Foundation, Zhejiang, Key R&D Program of Zhejiang (2024SSYS0031), and the National Natural Science Foundation of China (project No. 32170961).

Author contributions

J.-M.J. conceived the project, designed the experiments, and supervised this study. J.R. did primary experiments, obtained and organized the majority of original data, and wrote the manuscript draft. X.Q. participated in behavioural assay design and operations, siRNA cisterna magna injection, gut health inspection assay, BBB integrity inspection, caldesmon expression inspection, cluster analysis of similarity index, and wrote Mann-Whitney U test R code. Y.Z.wrote the main MATLAB code for PI. H.X. participated in the looming assay and VR_{eagle} assay, as well as in blood pressure measurement and long-term whisker stimulation. D.Z. provided primer pairs of *Grin1*, raw data of electron microscope, and *SMA-creER:Grin2d*$^{f/f}$ OFT_40*40 data. W.W. contributed to the writing of MATLAB code with Y.Z.. B.Z. participated in the genotyping of mice and cell sorting. D.L. helped the mouse brain section.

Declaration of interests

The authors declare no competing interests.

Supplemental information

Supplemental figures: Figures S1-S18

Supplemental tables: Tables S1-S3

Supplemental videos: Videos S1-S2

Figure legends

Figure 1. Artificial reduction of rCBF *de novo* initiates emotion. (A) The schematic diagram of the potential route linking neural signals initiated by arteriolar optogenetics in the BLA and ended in defecation behavior. (B-C) c-Fos^{+} neuron density and fecal pellet quantification after experiencing 15-min tube stress in the two groups of mice with IP injection of saline or C21. Both groups received *AAV2/5-hM4D (Gi)-EGFP* virus injection in their BLA. One dot represents one mouse. (D) Fecal pellet quantification for two groups of mice received the same treatment as C, except for the experience of 15-min OFT instead of tube stress (N =9 mice for each group). (E) The spatial map of defecation locations in the OFT from a total of 27 mice. (F) The percentage of defecation and traveling time behavior occurred in the center versus peripheral

areas in the OFT box (N =27 mice). (G) Optical photometry recording of fluorescent intensity in the BLA of mouse received multiple orbital injections of four doses of Rhodamine B. (H) Linear relationship between Rhodamine B concentration and plasma fluorescence intensity in G. (I) The timeline of the experiment of arteriolar optogenetic control and recording rCBF in the BLA. (J) Temporal dynamics of rCBF changes before, during, and after arteriolar optogenetics with four different stimulation protocols (see Methods). (K) The quantified area under the curve (AUC) for J. Each dot represents one mouse. (L) The fluorescence decay curve in the BLA of awake mice after receiving orbital Rhodamine B injection. (M) Quantification of rCBF changes in the BLA across three consecutive 15-minute recordings. Arteriolar optogenetics was applied during the second 15-minute recording. mice. (N) The quantification of AUC for M. N =8 *SMACreER:Ai47* (ChR2$^-$) mice, N =7, *SMACreER:Ai32* (ChR2$^+$) mice. (O-P) Defecation behavior quantifications upon optical and tube stress stimulations. The defecation rates of mice within a 45-minute period in the home cage or tube stress assay in O. The fecal production every 15 min in P. N =14, 7, and 10 mice for each group, respectively. (Q) Representative image of co-staining of c-Fos and NeuN in the BLA from ChR2$^-$ or ChR2$^+$ mice. (R) The quantification for Q. (S) Real-time rCBF changes in the BLA of mice before and during OFT in S. N =4 mice. (T) The quantification for S. (U-Y) Quantifications of behaviors of ChR2$^-$ or ChR2$^+$ mice while receiving optical stimulation during OFT. Quantifications of defecation rate, feical production

and defecation latency in U-W. Quantifications of the total running distance and the time spent in the center of the OFT box in X and Y. N =4 mice for each group. Data are presented as mean ± SEM. See also Figure S1, Table S1 and S2. Student's t-test was used for differential analysis of all data, except for fecal particles, using the Mann-Whitney U test. ****P<0.0001.

Figure 2. Establishment of various genetic lines of NVC deficiency and evaluations of their emotional responsiveness (A) The schematic of NsMJ in NVU. (B) mRNA expressions of NMDAR subunits in cerebral parenchymal aSMCs. (C) The quantification for B. N =3 independent experiments. (D) RNAscope of *Grin2d* transcripts (green dots) in *SMA-creER:Ai14* mouse brain section. The white arrow points to *Grin2d*mRNA present in aSMC (red), the relative location shown in the inserted histogram. (E-F) GluN2D and Smoothelin protein expressions in arterioles. The quantification in F (N =11-12 aSMCs from 4 arterioles of 4 mice for each genotype). (G) GluN2D expressions in the sorted aSMCs ($EGFP^{+}$) from *SMA-creER:Ai47* and *SMA-creER:Ai47:Grin2d*$^{f/f}$ mice. N =3 biological replicates. (H) GluN2D expressions in the cerebral tissue. N =3 biological replicates. (I) rCBF changes in the BLA before and during OFT. The vertical black dash line marks OFT begin. The vertical colour dash lines mark defecation time point. Inserted, basal levels of rCBF at home cage. N =4 mice for each group. Figure 1S and Figure 2I shared the same raw data for *Grin2d*$^{f/f}$ mice. (J) Quantification of the

934 1st 5-min rCBF area under the curve (AUC) for I. (K) Total fecal production
935 within a 15-min OFT or tube stress, and 24 hrs home cage. Underlined
936 numbers mean defecation rate (%), under which the numbers mean fecal
937 particles averaged from total mice for each group. The mouse number (N) for
938 each group is shown along the genotype in the X axis. Inserted panel is the
939 food consumption of control/HFD mice in 24 hrs (N =16 mice for each group,
940 each dot presents the mean value of one cage contains 4 mice). (L) Heatmap
941 of the relationship between the extent of NVC and EI_defecation. (M)
942 Cumulative defecation latency from 14 mice for each genotype subjected to
943 the OFT. (N) Fecal production within every 5 min during the 15-minute OFT. N
944 =14 and 16 for each genotype). (O) Defecation rates after OFTs with different
945 floor areas and after tube test. (P) Fecal particles for D. Raw data of *Grin2d*$^{f/f}$
946 and *SMA-creER:Grin2d*$^{f/f}$ was shared in K-P. N =12-19 mice shown in O.
947 (Q)Top 10 KEGG pathways of the Glu2D-binding protein complex. N =3
948 experiments. (R) Western blottings of GluN2D and Caldesmon using samples
949 pulled down by anti-GluN2D. N =3 independent experiments. (S) *Cald* mRNA
950 expression in the cortex lysis with cisterna magna injection of *Cald* siRNA or
951 scramble, N =3 biological replicates. (T) LSCI imaging of CBF changes of mice
952 with the same treatment as in U before receiving whisker stimulation. Insert,
953 quantification for mean changes in CBF. N =5-6 mice for each group. (U) The
954 immunofluorescence staining of Caldesmon of mice received local BLA siRNA
955 injection. (V) Quantifications for U and for Figure S9A. Dots represent mouse

numbers. Student's t-test was used for differential analysis of all data, except fecal particles used the Mann-Whitney U test. Data are presented as mean ± SEM. See also Table S1-S3 and Figures S2-S11. ****P<0.0001.

Figure3. Neural mechanism for NVC deficiency induced hyper-responsiveness. (A) Representative images of c-Fos immunostaining in the BLA mice received OFT. (B) Quantifications of c-Fos^{+} neuron density for A. Each dot represents one mouse. (C) Ca^{2+} changes in BLA before and during OFT. (D) Quantification for C. (E) The fecal production of *SMA-creER:Grin2d*$^{f/f}$ mice with hM4D (Gi) expressed in the BLA excitatory neurons. N =8 mice received IP injection of saline, and N =7 mice received C21. (F) Diagram of *Piezo2* KD virus infection range in BLA. (G-I) Before and during OFT, real-time neural activity recordings in the BLA where stereotactic injection with scramble or *Piezo2* siRNA as well as quantification of defecation behaviors in OFT. Ca^{2+} changes in G and H. Fecal production in I. N =8 mice for each group. Student's t-test was used for differential analysis of all data, except fecal particles used the Mann-Whitney U test. Data are presented as mean ± SEM. See also Table S1, S2, and Figure S12. ****P<0.0001.

Figure 4. Prediction platform for estimating false emotions. (A) Prediction index-based unbiased classification of stress levels for seven contexts. (B-G) The predicted position of every single treatment in the unbiased classification

system. The stress levels are denoted as Level_0 (blue), Level_1 (green), Level_2 (yellow), and Level_3 (brown). See also Table S1, Figure S13 and Figure S14.

Figure 5. NVC deficiency prompted an early relaxation of defense upon predator-like attack. (A-D) Looming assay. Temporal profile of locomotion speed dynamics of the two genotypic mice before (cyan) and during (yellow) stimulation in A. Heatmap that profiled the locomotion speed dynamics for a total of 30 seconds in B. The yellow box marks the 3-sec looming duration. Cumulative time used for relaxation from a freezing status following looming stimulation in C. Rearing index of each group in D. N =15 mice for each group. (E-G) VR_{eagle} stimulation. Temporal changes of the normalized pupil size and locomotion speed during and after VR_{eagle} stimulation in E. Eagle screech only present during the first 1.5s (blue) and eagle started to dive at 1.5 second. Representative images of VReagle video and mouse eye with pupil clear visualized. The statistical data of the initial phase of step_5 for E in F. The statistical data of pupil size full-recovery latency and looming locomotion full-recovery latency in G. For VR_{eagle}, N =7 mice for each group; for Looming, N =15 mice for each group. (H-L) Cat_{video} assay. The locomotion pattern during the Cat_{video} assay in H. Black bar marks retreat behavior; magenta lines indicate tail rattling. Two vertical dash lines highlight the time points when the cat appeared and pounced. Mouse numbering is on the left. Quantification of

retreat behaviors of *Grin2d*$^{f/f}$ mice before and after cat appearance in I. Retreat rate of two groups upon in Cat_{video} stimulation in J. Retreat rate referred to the fraction of mice that exhibited at least one retreat behavior of total mice. Dark green means retreat exhibited; light green means no retreat. Cumulative retreat time curve in K. Quantification of tail rattling times in L. N =12 mice for each group. Student's t-test was used for differential analysis of all data. Data are presented as mean ± SEM. See also Table S1, Figure S14-S16, and Supplementary Video 1 and 2.

Figure 6. NVC-deficient mice are predicted to hypo-respond to real social stress. (A) Picture of a home cage from a side view. (B) The total fighting time. (C-D) The predicted positions of the two genotypic miceexperience social stress. (E) The total time of staying with CD1 mouse in the small space. (F-G) The flee rate of *Grin2d*$^{f/f}$ and *SMA-creER:Grin2d*$^{f/f}$ mice (counted as per mouse) after fighting in F, and the normalized flee rate (counted as per fight event) after each fighting in G. (H) The sniffing times. N =8 and 10 mice for *Grin2d*$^{f/f}$ and *SMA-creER:Grin2d*$^{f/f}$). Student's t-test was used for differential analysis of all data, except fecal particles used the Mann-Whitney U test. Data are presented as mean ± SEM. See also Table S1.

Figure 7. The NVC-enhancement model resisted emotion rigidity following chronic restraint stress. (A)RNAscope of *Glrb* transcripts in brain

slices of *Pdgfrβ-creER:Ai14* mice. (B) Quantification of mRNA signal dots in aSMCs and vSMCs for A. N =41 aSMCs and N =32 vSMCs from a total of 3 brain sections of each mouse. N =4 mice for each group. (C) GlyR*β* protein expression in arterioles and venules from two genotypic mice. (D) Quantification of GlyR*β* clusters in aSMCs and vSMCs in C. N =14 arterioles, N =19 venules. n=6 mice for each group. (E) Quantification of GlyRβ immunosignal intensity for C (n=6 mice for each group). (F) Semi-quantitative analysis of *Glrb* mRNA by RT-PCR for the sorted PDGFRβ^{+} cells in the cerebral cortex. (G) Co-immunostaining of GlyR*β* and Gephyrin in HUvSMC cell line. The white arrow marks their colocalizations. Insert, the statistical co-localization analysis (N =4 cells). (H) Representative image of glycinergic NsMJ in a venule. Insert, histogram analysis of the location indicated by the white arrow. (I) Serial SEM sections of the ascending venule in mouse cerebral cortex. The white arrows point to axon's boutons. (J) LSCI imaging of CBF changes in the barrel cortex upon whisker stimulation. (K) The mean changes in CBF for J. N =5-6 for each group. (L) The fecal production of mice in the OFT and tube stress assay. Defecation rate (underline) and mean fecal production. N =10-15 mice for each group. Figure 7J-7L used the raw data. Data of of *Pdgfrβ-creER:Grin2d*$^{f/f}$ mice from Figure 2K and Figure S6A. (M) Quantification of time spent in open arms of EPM and the Modified Bristol Score on the last day of CRS. N =6 control mice, N =13 mice for CRS group). (N) Representative images of stools with different Modified Bristol Scores.

(O-P) Progressive changes following CRS. Dynamic changes in Modified Bristol scores in O. Fecal particle number produced within a period of 60 min in P. N =6 mice for *Glrb*$^{f/f}$_Sham group, N =14 mice for *Glrb*$^{f/f}$ group received CRS, N =7 mice for *Pdgfrβ-creER:Glrb*$^{f/f}$ group received CRS. The evaluation was performed before the assay and once a week during CRS. (Q) Quantification of immobility time in the 5-minute FST. N =7 mice for *Glrb*$^{f/f}$ group, N =4 mice for *Pdgfrβ-creER:Glrb*$^{f/f}$ group. ****P<0.0001. Student's t-test was used for differential analysis of all data, except fecal particles used the Mann-Whitney U test. Data are presented as mean ± SEM. See also Tables S1-S3, Figure S17 and Figure S18. ****P<0.0001.

Methods

Animal and animal care

All mouse procedures complied with the Institutional Animal Care and Use Committee (IACUC) guidelines of the School of Life Sciences, Westlake University. All mice were housed in the Westlake University Laboratory Animal Resource Centre with standard animal facilities, which provided a 12-hour light/dark cycle at 25 °C. No more than six mice were fed in each cage, and standard chow/water was provided to the mice *ad libitum*. All the genetic information of mice is in Table S1.

Tube stress assay (ARS & CRS)

A 50ml tube was used to restrain the mice[46,77] to perform acute restraint stress (ARS) and chronic restraint stress (CRS). The tube cover and wall will be drilled to ensure normal breathing. For ARS, the mice were restrained in the tube for 15 min, and then the fecal production was measured. For the ARS plus chemogenetic manipulation assay, the C21 intraperitoneal injection was 45 min before the tube stress assay. After the assay, mice were fed alone in a clean new cage for 90 min and then used for brain extraction to detect c-Fos expression. For CRS, the mice were restrained in the tube for 120 min/day, constant for 28 days, and fecal production and Modified Bristol Score (Add “0” to indicate no defecation) was measured at the end of each seven days within 60 minutes in a home cage box.

Immunofluorescence staining

For Immunofluorescence (IF) staining, after anesthesia with 1% pentobarbital sodium, the mice were perfused with 1X PBS (5 min) and 4% PFA in 1X PBS (5 min) through the left ventricle to empty blood and fix tissue. Afterwards, tissue was extracted and fixed by 4% PFA in 1X PBS for 6 hours at 4 °C. For samples like the brain and peripheral organs, samples were sliced into 50 μm (Leica, Histo-VT1200S, DEU). Then, treated samples with 1% Triton X-100 (Diamond, Cat# A110694-0500, CHN) and 0.25% NDS (Jackson Resources, Cat# 017-000-121, USA) in 1X PBS for 60 min at room temperature. After that,

samples were rewashed three times with 1X PBS.

In the staining process, the primary antibody diluted with 0.1% Triton X-100 in 1X PBS was used to incubate samples overnight at 4 °C. After the incubation, samples were washed with 1X PBS 10 min (3 replicates). The corresponding secondary fluorescence-conjugated antibody diluted with 0.1% Triton X-100 in 1X PBS was used to incubate samples for 120 min at room temperature. After the incubation, samples were washed with 1X PBS for 10 min (3 replicates). After that, 1000X diluted DAPI (Beyotime, Cat# C1002, CHN) was used for nucleus staining. Finally, samples were covered by a glass slice with the mounting medium (SouthernBiotech, 0100-01, USA). Zeiss LSM800 (Zeiss, LSM800, DEU) microscopy was used for photography. A list of antibodies is in Table S2.

Open field test

The setup of open field test (OFT) referred to published papers.[34,78] Each mouse was placed in the central area of a 40*40 cm, 35*35 cm, or 10*10 cm box for the OFT. The camera recording was 15 min. For the chemogenetic manipulation assay, the C21 intraperitoneal injection was 45 min before the OFT. After the assay, mice were fed alone in a clean new cage for 90 min and then used for brain extraction to detect c-Fos expression. For the BLA CBF and calcium signal recording, optic fibers were implanted at BLA (AP: -1.6 mm; ML: +/-3.45 mm; DV: -4.0 mm) with the injection of hSyn-Gcamp-8f virus

(*SMA-creER:Ai32* mice do not need virus injection. Detailed information about virus mentioned later) two weeks before the assay. Before the formal assay, three days of adaptation were performed. On the day of the assay, orbital injection of Rhodamine B 100 μl 5 mg/ml 15 minutes before the recording. 405 nm light was used for bassline control, 488 nm light recording for the Gcamp-8f signal (For *SMA-creER:Ai32* mice, using 473 nm light for optogenetic stimulation), and 580 nm light recording for the Rhodamine B signal. Recording sustained 15 (For CBF and Ca^{2+} signal recoding)/45 minutes (For *SMA-creER:Ai32* mice).

Tamoxifen administration for mice

Tamoxifen (MCE, Cat# HY-13757A, USA) was dissolved in corn oil (Aladdin, Cat# C116023-500ml, CHN) and orally administered to mice (10 mg/ml, 200 μl per mouse per day). For *Acta2* cKO, tamoxifen was given from P21 to P24. Otherwise, tamoxifen was orally administered to mice from P60 to P63.

Optogenetic stimulation and recording

Optogenetic stimulation referred published papers.[23,79] *SMA-creER:Ai32* and *SMA-creER:Ai47* mice were used for optogenetic stimulation. Tamoxifen was administered to mice 18 days before tha assay. Then, optic fibers were implanted at BLA (AP: -1.6 mm; ML: +/-3.45 mm; DV: -4.0 mm) two weeks before the assay. Before the formal assay, three days of adaptation were

performed. On the day of the assay, orbital injection of Rhodamine B 100 μl 5 mg/ml (Sigma, Cat# R9379-1G, USA) 15 minutes before the recording. 405 nm light was used for bassline control, 580 nm light recording for Rhodamine B signal for 45 min, and 473 nm light for optogenetic stimulation was performed at the 2nd 15 min of the 45 min recording. The parameters of the stimulation protocol included the stimulation period, interval period, recording period, total frequency, and laser power. The optimal protocol shown in Figure 1J is 85 ms stimulation, 5 ms interval, 5 ms recording, 10 Hz frequency, 0.939 mW laser power. During the 45-minute recording, mice always stayed in their home cage, but all fecal particles were removed before the assay. After 45 min recording, fecal particles were recorded.

Cell culture

SMA-creER:Ai47 P0 mice were anesthetized with ice. Surgical tweezers were used to quickly extract the cortex and then transfer it into the 0.25% Trypsin (Thermo Scientific, Cat# 25200072, USA) for 15 min at 37 °C. Next, FBS (Gibico, Cat# 10099, USA) was added to block digestion. Then, cells were filted by a 40 μm filter (Falcon, Cat# 352340, CHN). Finally, cells were centrifuged 1,600*g at 4 °C for 5 min and resuspended by SMCM (ScienCell, Cat# 1101, USA) in T25 flasks (Corning, Cat# 430639, USA). When cells reached approximately 80% full of the bottom surface of T25 flasks, tamoxifen was administrated to cells. Tamoxifen was dissolved in DMSO (Solarbio, Cat#

D8371, CHN), and the final concentration of tamoxifen was 5 μM. After a four-day culture, EGFP in cells were expressed. Cells were sorted by MA-900 (Sony, FCCF-MBR, JPN) to obtain $EGFP^+$ cells. Sorted cells were cultured in SMCM for further assay. The purity of cells sorted by the same method was verified in a paper published by our laboratory.[19] For data in Figure 7F, samples were directly sorted from $Pdgfr\beta^+$ cells in brain lysis by using Anti-Pdgfrβ antibody (without cell culture). Then, $Pdgfr\beta^+$ cells were quickly resuspended by Trizol (Sangon Biotec, Cat# B511311-0100, CHN) for RNA extraction. A list of antibodies is in Table S2. In Figure 7G, Human Umbilical Vein Smooth Muscle Cells (HU-vSMC, Sciencell, Cat# 8020, USA) were used for cell culture.

RT-PCR

For cultured cells, after obtaining pure sorted $EGFP^+$ cells from the cortex, cells were cultured in 6 cm dishes (Corning, Cat# 430166, USA) with SMCM. After cells reached around 90% density, Trizol was used for the RNA extraction. For brain tissue, after mice were anesthetized with ice, the cortex or cerebellum of the mice was directly taken out, and TRIzol was used for RNA extraction. After extraction, all RNA samples were reverse transcribed to cDNA (50 ng/μl) using HiScript III 1st Strand cDNA Synthesis Kit (Vazyme, Cat# R312-02, CHN). For the Real-Time Polymerase Chain Reaction (RT-PCR), each reaction contained 10 μl of Green Taq Mix (Vazyme, Cat# P131-AA,

CHN), 2 μl of cDNA, 2 μl of primer pairs (10 μM), and 6 μl of RNAase-free water. Agarose gel electrophoresis used 2 % agarose gel (BIOWESTE, Cat# 111860, ESP) and ran at 220 V for 30 min. RT-PCR gel images were obtained from a Tanon imager (Tanon, 1600 Geil imager, CHN). A list of primer pairs is in Table S3.

RNAscope in situ hybridisation

Horizontal sections (15 μm) of tamoxifen administrated *SMA-creER:Ai14* (for *Grin2d*), *Pdgfrβ-creER:Ai14* (for *Glrb*) and C57/B6 *wild-type* (for *Grin2d* and *Grin1* probe validation) mice brains were obtained by CM1950 (Lecia, Histo-CM1950, DEU). All RNA scope *in situ* hybridisation productions were obtained from ACDbio, including RNAscope Multiplex Fluorescent Reagent Kit v2 (ACDbio, Cat# 323100, USA), *Grin2d* probe (ACDbio, Cat# 425951-C3, USA), *Grin1* probe (ACDbio, Cat# 431611, USA), and *Glrb* probe (ACDbio, Cat# 1225261-C1, USA). All operations were carried out following the reagent instructions of ACDbio company and the published paper.[19,80]

Western-bolt

For tissue sample collection, samples were ground with RIPA (Thermo Scientific, Cat# 89901, USA) in the tube on ice for 30 min. For cells, after they reached around 90% density, the RIPA was used for protein extraction on ice for 30 min. Protease Inhibitor Cocktail (CWBIO, Cat# CW22008, CHN) was

added into RIPA to prevent protease. After that, samples were centrifuged at 12,000*g at 4 °C for 5 min, and the supernatant was collected. Concentrations of proteins were measured by Micro BCA Protein Assay kit (CWBIO, Cat# CW2011S, CHN), and all samples were boiled with SDS-PAGE loading buffer (CWBIO, Cat# CW0027S, CHN) for 10 min at 100 °C. 8% SDS-polyacrylamide electrophoresis gels were used for gel running. After 90 min, gels running at 120 V (80 V for the first 30 min), gels were transferred to 0.45 μm PVDF membranes (Millipore, Cat# IPVH00010, USA) at 400 mA for 120 min. After transfer, PVDF membranes were blocked by 5% non-fat milk in 1X TBST buffer for 60 min at room temperature with a mild horizontal shake.

After the block, the primary antibody diluted with 5% non-fat milk in 1X TBST buffer was used to incubate the membrane overnight at 4 °C with a mild horizontal shake. After the incubation, the membrane was washed by 1X TBST 10min (3 replicates). The corresponding secondary HRP-conjugated antibody diluted with 5% non-fat milk in 1X TBST buffer was used to incubate the membrane for 45 minutes at room temperature with a mild horizontal shake. After the incubation, the membrane was washed with 1X TBST for 10 min (3 replicates). ECL kits (Abbkine, Cat# BMU102-CN, CHN) and gel image system (GE, GEL Imaging System AI680RGB v.2.0, USA) were used for exposure photography. A list of antibodies is in Table S2.

Whisker stimulation

Mice were anaesthesia with 1% pentobarbital sodium and open the scalp, then mice stable fixated on the holder. The electro-motor-driven brush stimulated the whisker longitudinally for 1 minute at a frequency of 12 Hz. The principle of laser speckle contrast imaging has been described in the previous paper,[24] and the operation referred to in the published paper.[38,81,82] Laser Speckle Image System (RWD, RFSLI ZW/RFSLI III, CHN) was used to record the CBF change in the ROI of the opposite barrel cortex of mice. The recording parameters were 512*512 resolution, 10 FPS, and 2-minute recording.

Immunoprecipitation assay

tdTomato^{+} sorted aSMCs from P0 *SMA-creER:Ai14* mice were used for lentivirus infection and further immunoprecipitation (IP) assay. Sorted cells were cultured in 6 cm dishes with SMCM. After cells reach around 90% density, add lentivirus (Lenti-EF1-EGFP-CMV-grin2d-3XFlag-WPRE) into the culture and keep for one week to over-express GluN2D. MA-900 sorted out EGFP and tdTomato double-positive cells, which were lentivirus-infected aSMCs. These cells were then cultured in 10 cm dishes. After cells reached around 90% density, cells were collected by RIPA reagent. The Protein G Magnetic beads kit (Epizyme, Cat# YJ002, CHN) was used for the immunoprecipitation assay. GluN2D and IgG control antibodies were mixed with Protein G Magnetic beads to pull down GluN2D and its related protein. Pull-down products were verified by western-bolt and analyzed through mass spectrometry. A list of antibodies

is in Table S3.

siRNA cisternal magna/BLA local injection

Cisterna magna injection protocol referred to Cannula Implantation into the cisterna magna of Rodents (https://doi.org/10.3791/57378) and paper published by our laboratory.[19] 1 nM siRNA was mixed with FITC (10 mg/ml, Sigma, FD40S-1G, USA) for injection (20 μl in total). The scalp was opened 10 min after the injection, and the microscope was used to detect the FITC signal (Zeiss, Axio Zoom v16, DEU) in perivascular spaces. Only successfully injected mice remain. Whisker stimulation was performed 48 hours after siRNA injection, followed by OFT_40*40. As for BLA local siRNA injection, 150nl of 1nM siRNA was injected in two sides of BLA (AP: -1.55 mm; ML: +/-3.40 mm; DV: -4.00 mm), and OFT_40*40 was performed 48 hours after siRNA injection. Brain slice collection was performed 90 minutes after OFT for IF staining. Sequence of siRNA can be found in the Table S3.

High-fat diet challenge assay

Set up of High-fat diet challenge referred to published papers.[41,43,83] Mice were given high-fat food (SYSE, Cat# PD6001, CHN) for four weeks. The weight of mice and food consumption were measured before the assay and at the end of each week. The home cage fecal production was measured using the same method mentioned in the “Home cage monitor assay” part. OFT_40*40 assay

and whisker stimulation assay were performed after four weeks of HFD challenge.

Home cage monitor assay

The blood pressure of mice was measured by Kent Noninvasive blood pressure measurement system for animals (Kent/Biopac, USA) before the mice were put into the home cage. Each home cage only contains four mice. In each cycle (three days), 60 g of food, 340 g of water (including bottle weight), and 100 g of padding were provided. Weight of mice, food/water consumption, fecal particles, and urination amount (counted by increased padding weight) were measured by calculating the mean data. Three cycles of monitoring were performed for each home cage. After the assay, mice were fed alone in a clean new cage for 90 min and then used for brain extraction to detect c-Fos expression. The intestine system inspection was performed after three cycles of monitor.

BBB leakage inspection (evens blue and IgG)

Assay setup referred to published papers.[43,84] 2% evens blue (Merck, Cat#E2129, USA) dissolved in saline was used for orbital injection (4 ul/g). After 45 min, the mouse was anesthetized, and the brain was extracted for appearance inspection for BBB leakage using a microscope (Zeiss, Axio Zoom v16, DEU). The brain was weighted and then homogenized using 1 ml of 50%

trichloroacetic acid (Merck, Cat#190780, USA). Then, samples were centrifuged at 10,000*g at 4 °C for 20 min, supernatants were collected, and absorbance detection at 620 nm was performed. For IgG inspection methods, see the *Immunofluorescence staining* part above.

Colorectal inspection

The ENDOQ Colonoscopy system took representative images of colorectal tissue. A professional physician performed scoring of the endoscopic images in a double-blind manner to ensure unbiased assessment.

Hematoxylin and eosin staining

For hematoxylin and eosin (HE) staining, after anesthesia with 1% pentobarbital sodium, the mice were perfused with 1X PBS (5 min) and 4% PFA in 1X PBS (5 min) through the left ventricle to empty blood and fix tissue. Afterward, tissue was extracted and fixed by 4% PFA in 1X PBS for 6 hours at 4 °C. After a paraffin block, tissues were sliced into 8 μm sections and examined following HE staining.

In vivo virus injection

rAAV2/4-Glyt2-EGFP-WPRE-hGHpolyA (5E+12VG/ml) was used to label glycinergic neurons. Two weeks before the assay, bilateral medullary reticular formation injection (500 nl on each side, AP: -3.5 mm; ML: +/-0.84 mm; DV:

-2.8 mm) was administered.[75] AAV2/5-mCaMKIIa-hM4D(Gi)-EGFP-ER2-WPRE-pA(2.30E+12VG/ml) and AAV2/5-mCaMKIIa-EGFP-ER2-WPRE-pA(2.30E+12VG/ml) were used for the chemogenetical manipulation. Two weeks before the assay, bilateral amygdala injection (150 nl on each side, AP: -1.6 mm; ML: +/-3.45 mm; DV: -4.1 mm) was administered.[85] AAV2/9-hSyn-jGCaMP8f-WPRE-pA was used for the neural calcium measurement. Two weeks before the assay, bilateral amygdala injection (150 nl on each side, AP: -1.6 mm; ML: +/-3.45 mm; DV: -4.1 mm) was administered. rAAV2/9-CamKIIa-3xflag-5'miR-30a-shRNA (piezo2)-3'-miR30a-WPREs and rAAV2/9-CamKIIa-3xflag-5'miR-30a-shRNA (scramble)-3'-miR30a-WPREs were used for the BLA local *Piezo2* KD. Two weeks before the assay, bilateral amygdala injection (100 nl Piezo-2 virus + 100 nl jGCaMP8f virus) on each side, AP: -1.6 mm; ML: +/-3.45 mm; DV: -4.1 mm) was administered.

Prediction Index (PI)

The Prediction Index (PI) is based on the Structural Similarity Index (SSIM) and the cluster analysis of SSIM (See Statistical analysis software and code part for details). In brief, translating BLA's c-Fos positive cells location and density with different contexts into SSIM. Then, the cluster analysis was used to classify the SSIM of different contexts to build a library of PI. To predict a subject's "real" stress level, the SSIM of this subject will be clustered together

with the PI library to locate the subject's stress level.

Complex-Open field test (c-OFT)

The complex-open field test (c-OFT) setup referred to a published paper.[45,86] Each mouse was placed in the central area of the left part of the c-OFT box. One side of the c-OFT box has a white bottom (the mouse is put on this side) and a black bottom on the other. The camera recording was 20 min. For the analysis, the box was divided into three parts (left area, central area, and right area) to analyze the preference of mice for metal fence (right area close to the metal fence). After the assay, mice were fed alone in a clean new cage for 90 minutes and then used for brain extraction to detect c-Fos expression.

Looming assay

The assay was carried out in a 35 cm*35 cm OFT box. The settings of the assay were based on the published paper.[49] Modifications include: Modifications include:

- mice will be put in the OFT box to adapt for 10 minutes before starting the assay;
- we only use a single camera at the top of the box to record;
- we stimulate the mice when they move and are not close to the box wall rather than continuously stimulating them.

Each mouse performs three trials of stimulations. After the assay, mice

were fed alone in a clean new cage for 90 min and then used for brain extraction to detect c-Fos expression.

VR_{eagle} assay

Assay set up referred published paper.[49] The mouse head was fixed with a fixator two weeks before the assay. The mice received daily adaptive training on the VR system one week before the assay. On the day of the assay, the mice were fixed on the VR system and given 5 min of adaptation. Unless stimulated, the screen in front of the mouse will always play the regular landscape video. The stimulation of the eagle lasts for three seconds. The eagle dives down from far to near and plays the voice of the eagle at the beginning of the stimulation. There were five trials of stimulation in total, and the criterion for the first stimulation was that the mice moved for the first time after 5 min of adaptation. The criteria for subsequent stimulation were that the last stimulation ended for at least 2 min, and mice resumed movement. The assay ended 2 min after the last stimulation. The pupil changes (Supplementary Video 1) and mice's locomotion speed were recorded simultaneously. After the assay, mice were fed alone in a clean new cage for 90 min and then used for brain extraction to detect c-Fos expression.

Cat_{video} stimulation assay

The assay was carried out in a 40*40 cm OFT box. The mouse head was fixed

with a fixator and trained to fit the treadmill two weeks before the assay. On the day of the assay, the mice were anesthetized with isoflurane and fixed on the treadmill. After the mouse wakes up, play the video of cat hunting on the iPad Air (Apple. Cat# 3rd generation, USA) in front of the mouse (Supplementary Video 2). The stimulation video played three consecutive times, each stimulation lasting 30 seconds. A camera directly above was used to record the assay.

Home cage social assay

The setup of the Home cage social assay referred to published papers.[52,86-89] CD1 mice never exposed to *Grin2d*$^{f/f}$ or *SMA-creER:Grin2d*$^{f/f}$ mice were used for the assay. Before the assay, simultaneously put a single *Grin2d*$^{f/f}$ or *SMA-creER:Grin2d*$^{f/f}$ mouse and a CD1 mouse into a cage. The cage contains new padding and a metal lid on the top. One side of the metal lid is used to place food and water bottles, so the height is lower than the other. A camera was used to record two mice's behaviours for 10 min. After the assay, the mice were separated again. *Grin2d*$^{f/f}$ or *SMA-creER:Grin2d*$^{f/f}$ mice were fed alone in a clean new cage for 90 min and then used for brain extraction to detect c-Fos expression.

Elevated plus-maze test

The setup of elevated plus-maze (EPM) referred to published papers.[80,90] The

EPM comprises two open arms (65*5 cm) and two close arms (65*5 cm). Each mouse was placed in the centre, facing one of the two open arms, and allowed to explore for 5 min. Time spent in open arms was recorded.

Serial block-face scanning electron microscopy image

The specimen was obtained in the same batch as the previously published paper from our laboratory.[19] The details in the “SBF-SEM imaging” section of the methods in that paper. In brief, the ascending venule was identified using X-ray microscopy (Zeiss, XRM, Xradia 520 Versa, DEU) at ×4 and 80 kV magnification. The specimen adhered to an aluminium metal pin using conductive epoxy (Chemtronics, CW2400, USA). Then, it was further precisely trimmed into a block of 600*600*700 μm^3 using a glass knife and a right-angled diamond knife (DiATOME, Trim 90, CHE) after coating with gold-palladium (Leica, EM ACE200, DEU) and a final trim using a 3View ultramicrotome (Gatan, USA). Image acquisition was performed using a BSE detector on a Carl Zeiss Gemini 300 scanning electron microscope at 2 kV voltage and approximately 1.8*10−3 mBar in high-vacuum mode with focus charge compensation. The specimens were sectioned at a 50–75 nm thickness and a cutting speed of 0.1 mm/s.

Force Swimming Test (FST)

The Force Swimming Test (FST) referred to a published paper.[91] In brief, mice

were put into the glass water tank with 25 °C clear water. Measuring the swimming time of mice in 5 minutes and then putting the mouse back in the home cage.

Statistical analysis software and code

All the image processing and analysis of fluorescence intensity used Zeiss Zen Lite (v3.4) and ImageJ (v1.53u). All whisker stimulation original data were measured by RWD LSIS-self software (v5.0). All the original behavioral data for OFT/c-OFT/EPM were recorded using Noldus. Data recording and analysis of Looming and VR_{eagle} assay was performed using self-compiled codes provided by Bayonne company. All statistical data were processed by Numbers (v12.2). Unless otherwise specified, Student's t-test was used for differential analysis on all data that conform to a normal distribution. Non-continuous data that does not conform to a normal distribution, such as fecal particles, signal dots in vessels, and rearing index were analyzed using the Mann-Whitney U test. All figures were made by Prism (v9.4.1) and Adobe Illustrator 2024 (v28.3). CBF peak mean value, heat maps, mass spectrometry data inclusion criteria, cross-correlation, and prediction index (based on the Structural Similarity Index, SSIM) were analyzed by self-compiled MATLAB codes. Besides, the KEGG pathways, cluster analysis of SSIM, and Mann-Whitney U test were analyzed using self-compiled R code. All available codes can be found at

https://github.com/JialabEleven/Functional_hyperemia_regulates_emotion.

References

1. Bortolon, C., Chen, S., and Bonanno, G.A. (2023). Components of emotion regulation flexibility and psychosis: The association between psychosis-proneness and context sensitivity. Br J Clin Psychol *62*, 82-95. 10.1111/bjc.12395.
2. D'Agostino, A., Covanti, S., Rossi Monti, M., and Starcevic, V. (2017). Reconsidering Emotion Dysregulation. Psychiatr Q *88*, 807-825. 10.1007/s11126-017-9499-6.
3. Roelofs, K., Bramson, B., and Toni, I. (2023). A neurocognitive theory of flexible emotion control: The role of the lateral frontal pole in emotion regulation. Ann N Y Acad Sci *1525*, 28-40. 10.1111/nyas.15003.
4. McCracken, L.M. (2024). Psychological Flexibility, Chronic Pain, and Health. Annu Rev Psychol *75*, 601-624. 10.1146/annurev-psych-020223-124335.
5. Addolorato, G., Mirijello, A., D'Angelo, C., Leggio, L., Ferrulli, A., Abenavoli, L., Vonghia, L., Cardone, S., Leso, V., Cossari, A., et al. (2008). State and trait anxiety and depression in patients affected by gastrointestinal diseases: psychometric evaluation of 1641 patients referred to an internal medicine outpatient setting. Int J Clin Pract *62*,

1063-1069. 10.1111/j.1742-1241.2008.01763.x.

6. Easdale-Cheele, T., Parlatini, V., Cortese, S., and Bellato, A. (2024). A Narrative Review of the Efficacy of Interventions for Emotional Dysregulation, and Underlying Bio-Psycho-Social Factors. Brain Sci *14*. 10.3390/brainsci14050453.

7. Thompson, R.A. (2011). Methods and measures in developmental emotions research: some assembly required. J Exp Child Psychol *110*, 275-285. 10.1016/j.jecp.2011.04.007.

8. De Prisco, M., Oliva, V., Fico, G., Radua, J., Grande, I., Roberto, N., Anmella, G., Hidalgo-Mazzei, D., Fornaro, M., de Bartolomeis, A., et al. (2023). Emotion dysregulation in bipolar disorder compared to other mental illnesses: a systematic review and meta-analysis. Psychol Med *53*, 7484-7503. 10.1017/S003329172300243X.

9. Geng, H., Xu, P., Aleman, A., Qin, S., and Luo, Y.J. (2024). Dynamic Organization of Large-scale Functional Brain Networks Supports Interactions Between Emotion and Executive Control. Neurosci Bull *40*, 981-991. 10.1007/s12264-023-01168-w.

10. Szaflarski, J.P., Allendorfer, J.B., Heyse, H., Mendoza, L., Szaflarski, B.A., and Cohen, N. (2014). Functional MRI of facial emotion processing in left temporal lobe epilepsy. Epilepsy Behav *32*, 92-99. 10.1016/j.yebeh.2014.01.012.

11. Etkin, A., and Wager, T.D. (2007). Functional neuroimaging of anxiety: a

meta-analysis of emotional processing in PTSD, social anxiety disorder, and specific phobia. Am J Psychiatry *164*, 1476-1488. 10.1176/appi.ajp.2007.07030504.

12. Phillips, M.L., Drevets, W.C., Rauch, S.L., and Lane, R. (2003). Neurobiology of emotion perception II: Implications for major psychiatric disorders. Biol Psychiatry *54*, 515-528. 10.1016/s0006-3223(03)00171-9.

13. Mathias, E.J., Kenny, A., Plank, M.J., and David, T. (2018). Integrated models of neurovascular coupling and BOLD signals: Responses for varying neural activations. Neuroimage *174*, 69-86. 10.1016/j.neuroimage.2018.03.010.

14. Iadecola, C. (2017). The Neurovascular Unit Coming of Age: A Journey through Neurovascular Coupling in Health and Disease. Neuron *96*, 17-42. 10.1016/j.neuron.2017.07.030.

15. Pico-Perez, M., Radua, J., Steward, T., Menchon, J.M., and Soriano-Mas, C. (2017). Emotion regulation in mood and anxiety disorders: A meta-analysis of fMRI cognitive reappraisal studies. Prog Neuropsychopharmacol Biol Psychiatry *79*, 96-104. 10.1016/j.pnpbp.2017.06.001.

16. Drew, P.J. (2022). Neurovascular coupling: motive unknown. Trends Neurosci *45*, 809-819. 10.1016/j.tins.2022.08.004.

17. Masamoto, K., Hirase, H., Yamada, K., and Kanno, I. (2016).

Neurovascular coupling-What next? Prog Brain Res *225*, 269-272. 10.1016/bs.pbr.2016.03.007.

18. Dion-Albert, L., Dudek, K.A., Russo, S.J., Campbell, M., and Menard, C. (2023). Neurovascular adaptations modulating cognition, mood, and stress responses. Trends Neurosci *46*, 276-292. 10.1016/j.tins.2023.01.005.

19. Zhang, D., Ruan, J., Peng, S., Li, J., Hu, X., Zhang, Y., Zhang, T., Ge, Y., Zhu, Z., Xiao, X., et al. (2024). Synaptic-like transmission between neural axons and arteriolar smooth muscle cells drives cerebral neurovascular coupling. Nat Neurosci *27*, 232-248. 10.1038/s41593-023-01515-0.

20. Hill, R.A., Tong, L., Yuan, P., Murikinati, S., Gupta, S., and Grutzendler, J. (2015). Regional Blood Flow in the Normal and Ischemic Brain Is Controlled by Arteriolar Smooth Muscle Cell Contractility and Not by Capillary Pericytes. Neuron *87*, 95-110. 10.1016/j.neuron.2015.06.001.

21. Holstein-Rønsbo, S., Gan, Y., Giannetto, M.J., Rasmussen, M.K., Sigurdsson, B., Beinlich, F.R.M., Rose, L., Untiet, V., Hablitz, L.M., Kelley, D.H., and Nedergaard, M. (2023). Glymphatic influx and clearance are accelerated by neurovascular coupling. Nat Neurosci *26*, 1042-1053. 10.1038/s41593-023-01327-2.

22. Hartmann, D.A., Berthiaume, A.A., Grant, R.I., Harrill, S.A., Koski, T., Tieu, T., McDowell, K.P., Faino, A.V., Kelly, A.L., and Shih, A.Y. (2021).

Brain capillary pericytes exert a substantial but slow influence on blood flow. Nat Neurosci *24*, 633-645. 10.1038/s41593-020-00793-2.

23. Chao, T.H., Zhang, W.T., Hsu, L.M., Cerri, D.H., Wang, T.W., and Shih, Y.I. (2022). Computing hemodynamic response functions from concurrent spectral fiber-photometry and fMRI data. Neurophotonics *9*, 032205. 10.1117/1.NPh.9.3.032205.

24. Niwa, K., Araki, E., Morham, S.G., Ross, M.E., and Iadecola, C. (2000). Cyclooxygenase-2 contributes to functional hyperemia in whisker-barrel cortex. J Neurosci *20*, 763-770. 10.1523/JNEUROSCI.20-02-00763.2000.

25. Yang, G., Zhang, Y., Ross, M.E., and Iadecola, C. (2003). Attenuation of activity-induced increases in cerebellar blood flow in mice lacking neuronal nitric oxide synthase. Am J Physiol Heart Circ Physiol *285*, H298-304. 10.1152/ajpheart.00043.2003.

26. Ando, K., Tong, L., Peng, D., Vazquez-Liebanas, E., Chiyoda, H., He, L., Liu, J., Kawakami, K., Mochizuki, N., Fukuhara, S., et al. (2022). KCNJ8/ABCC9-containing K-ATP channel modulates brain vascular smooth muscle development and neurovascular coupling. Dev Cell *57*, 1383-1399 e1387. 10.1016/j.devcel.2022.04.019.

27. Shen, J., Wang, D., Wang, X., Gupta, S., Ayloo, B., Wu, S., Prasad, P., Xiong, Q., Xia, J., and Ge, S. (2019). Neurovascular Coupling in the Dentate Gyrus Regulates Adult Hippocampal Neurogenesis. Neuron

103, 878-890 e873. 10.1016/j.neuron.2019.05.045.

28. Hogan-Cann, A.D., Lu, P., and Anderson, C.M. (2019). Endothelial NMDA receptors mediate activity-dependent brain hemodynamic responses in mice. Proc Natl Acad Sci U S A *116*, 10229-10231. 10.1073/pnas.1902647116.

29. Chow, B.W., Nunez, V., Kaplan, L., Granger, A.J., Bistrong, K., Zucker, H.L., Kumar, P., Sabatini, B.L., and Gu, C. (2020). Caveolae in CNS arterioles mediate neurovascular coupling. Nature *579*, 106-110. 10.1038/s41586-020-2026-1.

30. Lee, C., Doo, E., Choi, J.M., Jang, S.H., Ryu, H.S., Lee, J.Y., Oh, J.H., Park, J.H., Kim, Y.S., Brain-Gut Axis Research Group of Korean Society of, N., and Motility (2017). The Increased Level of Depression and Anxiety in Irritable Bowel Syndrome Patients Compared with Healthy Controls: Systematic Review and Meta-analysis. J Neurogastroenterol Motil *23*, 349-362. 10.5056/jnm16220.

31. Sarro, E.C., Sullivan, R.M., and Barr, G. (2014). Unpredictable neonatal stress enhances adult anxiety and alters amygdala gene expression related to serotonin and GABA. Neuroscience *258*, 147-161. 10.1016/j.neuroscience.2013.10.064.

32. Suda, K., Setoyama, H., Nanno, M., Matsumoto, S., and Kawai, M. (2013). Involvement of parasympathetic pelvic efferent pathway in psychological stress-induced defecation. World J Gastroenterol *19*,

1200-1209. 10.3748/wjg.v19.i8.1200.

33. Gorard, D.A., Gomborone, J.E., Libby, G.W., and Farthing, M.J. (1996). Intestinal transit in anxiety and depression. Gut *39*, 551-555. 10.1136/gut.39.4.551.

34. Hale, M.W., Hay-Schmidt, A., Mikkelsen, J.D., Poulsen, B., Shekhar, A., and Lowry, C.A. (2008). Exposure to an open-field arena increases c-Fos expression in a distributed anxiety-related system projecting to the basolateral amygdaloid complex. Neuroscience *155*, 659-672. 10.1016/j.neuroscience.2008.05.054.

35. Gorski, J.A., Talley, T., Qiu, M., Puelles, L., Rubenstein, J.L., and Jones, K.R. (2002). Cortical excitatory neurons and glia, but not GABAergic neurons, are produced in the Emx1-expressing lineage. J Neurosci *22*, 6309-6314. 10.1523/JNEUROSCI.22-15-06309.2002.

36. Monyer, H., Burnashev, N., Laurie, D.J., Sakmann, B., and Seeburg, P.H. (1994). Developmental and regional expression in the rat brain and functional properties of four NMDA receptors. Neuron *12*, 529-540. 10.1016/0896-6273(94)90210-0.

37. Laurie, D.J., Bartke, I., Schoepfer, R., Naujoks, K., and Seeburg, P.H. (1997). Regional, developmental and interspecies expression of the four NMDAR2 subunits, examined using monoclonal antibodies. Brain Res Mol Brain Res *51*, 23-32. 10.1016/s0169-328x(97)00206-4.

38. Boas, D.A., and Dunn, A.K. (2010). Laser speckle contrast imaging in

biomedical optics. J Biomed Opt *15*, 011109. 10.1117/1.3285504.

39. Zhang, Y., Chen, K., Sloan, S.A., Bennett, M.L., Scholze, A.R., O'Keeffe, S., Phatnani, H.P., Guarnieri, P., Caneda, C., Ruderisch, N., et al. (2014). An RNA-sequencing transcriptome and splicing database of glia, neurons, and vascular cells of the cerebral cortex. J Neurosci *34*, 11929-11947. 10.1523/JNEUROSCI.1860-14.2014.

40. Foster, D.B., Shen, L.H., Kelly, J., Thibault, P., Van Eyk, J.E., and Mak, A.S. (2000). Phosphorylation of caldesmon by p21-activated kinase. Implications for the Ca(2+) sensitivity of smooth muscle contraction. J Biol Chem *275*, 1959-1965. 10.1074/jbc.275.3.1959.

41. Huber, G., Ogrodnik, M., Wenzel, J., Stolting, I., Huber, L., Will, O., Peschke, E., Matschl, U., Hovener, J.B., Schwaninger, M., et al. (2021). Telmisartan prevents high-fat diet-induced neurovascular impairments and reduces anxiety-like behavior. J Cereb Blood Flow Metab *41*, 2356-2369. 10.1177/0271678X211003497.

42. Yang, S., and Webb, A.J.S. (2024). Reduced neurovascular coupling is associated with increased cardiovascular risk without established cerebrovascular disease: A cross-sectional analysis in UK biobank. J Cereb Blood Flow Metab, 271678x241302172. 10.1177/0271678x241302172.

43. Chang, H.C., Tai, Y.T., Cherng, Y.G., Lin, J.W., Liu, S.H., Chen, T.L., and Chen, R.M. (2014). Resveratrol attenuates high-fat diet-induced

disruption of the blood-brain barrier and protects brain neurons from apoptotic insults. J Agric Food Chem *62*, 3466-3475. 10.1021/jf403286w.

44. Hochgerner, H., Singh, S., Tibi, M., Lin, Z., Skarbianskis, N., Admati, I., Ophir, O., Reinhardt, N., Netser, S., Wagner, S., and Zeisel, A. (2023). Neuronal types in the mouse amygdala and their transcriptional response to fear conditioning. Nat Neurosci *26*, 2237-2249. 10.1038/s41593-023-01469-3.

45. Shoji, H., and Miyakawa, T. (2021). Effects of test experience, closed-arm wall color, and illumination level on behavior and plasma corticosterone response in an elevated plus maze in male C57BL/6J mice: a challenge against conventional interpretation of the test. Mol Brain *14*, 34. 10.1186/s13041-020-00721-2.

46. Chen, M., Ma, S., Liu, H., Dong, Y., Tang, J., Ni, Z., Tan, Y., Duan, C., Li, H., Huang, H., et al. (2024). Brain region-specific action of ketamine as a rapid antidepressant. Science *385*, eado7010. 10.1126/science.ado7010.

47. Silva, B.A., Gross, C.T., and Graff, J. (2016). The neural circuits of innate fear: detection, integration, action, and memorization. Learn Mem *23*, 544-555. 10.1101/lm.042812.116.

48. Apfelbach, R., Blanchard, C.D., Blanchard, R.J., Hayes, R.A., and McGregor, I.S. (2005). The effects of predator odors in mammalian prey

species: a review of field and laboratory studies. Neurosci Biobehav Rev *29*, 1123-1144. 10.1016/j.neubiorev.2005.05.005.

49. Shang, C., Chen, Z., Liu, A., Li, Y., Zhang, J., Qu, B., Yan, F., Zhang, Y., Liu, W., Liu, Z., et al. (2018). Divergent midbrain circuits orchestrate escape and freezing responses to looming stimuli in mice. Nat Commun *9*, 1232. 10.1038/s41467-018-03580-7.

50. Lee, T., Weinberg-Wolf, H., Zapadka, T.E., Rudenko, A., Demb, J.B., and Kim, I.J. (2024). Specific retinal neurons regulate context-dependent defensive responses to visual threat. PNAS Nexus *3*, pgae423. 10.1093/pnasnexus/pgae423.

51. Wang, L., Chen, I.Z., and Lin, D. (2015). Collateral pathways from the ventromedial hypothalamus mediate defensive behaviors. Neuron *85*, 1344-1358. 10.1016/j.neuron.2014.12.025.

52. Bigi, S., Maestripieri, D., Aloe, L., and Alleva, E. (1992). NGF decreases isolation-induced aggressive behavior, while increasing adrenal volume, in adult male mice. Physiol Behav *51*, 337-343. 10.1016/0031-9384(92)90150-z.

53. Lee, S., Kang, B.M., Shin, M.K., Min, J., Heo, C., Lee, Y., Baeg, E., and Suh, M. (2015). Chronic Stress Decreases Cerebrovascular Responses During Rat Hindlimb Electrical Stimulation. Front Neurosci *9*, 462. 10.3389/fnins.2015.00462.

54. Chiba, S., Numakawa, T., Ninomiya, M., Richards, M.C., Wakabayashi,

C., and Kunugi, H. (2012). Chronic restraint stress causes anxiety- and depression-like behaviors, downregulates glucocorticoid receptor expression, and attenuates glutamate release induced by brain-derived neurotrophic factor in the prefrontal cortex. Prog Neuropsychopharmacol Biol Psychiatry *39*, 112-119. 10.1016/j.pnpbp.2012.05.018.

55. Vanlandewijck, M., He, L., Mae, M.A., Andrae, J., Ando, K., Del Gaudio, F., Nahar, K., Lebouvier, T., Lavina, B., Gouveia, L., et al. (2018). A molecular atlas of cell types and zonation in the brain vasculature. Nature *554*, 475-480. 10.1038/nature25739.

56. Froehner, S.C. (1993). Regulation of ion channel distribution at synapses. Annu Rev Neurosci *16*, 347-368. 10.1146/annurev.ne.16.030193.002023.

57. Lee, S., Kang, B.M., Kim, J.H., Min, J., Kim, H.S., Ryu, H., Park, H., Bae, S., Oh, D., Choi, M., and Suh, M. (2018). Real-time in vivo two-photon imaging study reveals decreased cerebro-vascular volume and increased blood-brain barrier permeability in chronically stressed mice. Sci Rep *8*, 13064. 10.1038/s41598-018-30875-y.

58. Liu, Y., Wu, Y., and Yang, Q. (2024). The impact of stress on the risk decision-making process. Psychophysiology *61*, e14595. 10.1111/psyp.14595.

59. Sandrone, S., Bacigaluppi, M., Galloni, M.R., Cappa, S.F., Moro, A.,

Catani, M., Filippi, M., Monti, M.M., Perani, D., and Martino, G. (2014). Weighing brain activity with the balance: Angelo Mosso's original manuscripts come to light. Brain *137*, 621-633. 10.1093/brain/awt091.

60. Roy, C.S., and Sherrington, C.S. (1890). On the Regulation of the Blood-supply of the Brain. J Physiol *11*, 85-158 117. 10.1113/jphysiol.1890.sp000321.

61. Eisenberger, N.I., Lieberman, M.D., and Williams, K.D. (2003). Does rejection hurt? An FMRI study of social exclusion. Science *302*, 290-292. 10.1126/science.1089134.

62. Guo, Y., Zou, G., Shao, Y., Chen, J., Li, Y., Liu, J., Yao, P., Zhou, S., Xu, J., Hu, S., et al. (2023). Increased connectivity of the anterior cingulate cortex is associated with the tendency to awakening during N2 sleep in patients with insomnia disorder. Sleep *46*. 10.1093/sleep/zsac290.

63. Cera, N., Di Pierro, E.D., Ferretti, A., Tartaro, A., Romani, G.L., and Perrucci, M.G. (2014). Brain networks during free viewing of complex erotic movie: new insights on psychogenic erectile dysfunction. PLoS One *9*, e105336. 10.1371/journal.pone.0105336.

64. Brom, M., Both, S., Laan, E., Everaerd, W., and Spinhoven, P. (2014). The role of conditioning, learning and dopamine in sexual behavior: a narrative review of animal and human studies. Neurosci Biobehav Rev *38*, 38-59. 10.1016/j.neubiorev.2013.10.014.

65. Hou, X.H., Hyun, M., Taranda, J., Huang, K.W., Todd, E., Feng, D.,

Atwater, E., Croney, D., Zeidel, M.L., Osten, P., and Sabatini, B.L. (2016). Central Control Circuit for Context-Dependent Micturition. Cell *167*, 73-86.e12. 10.1016/j.cell.2016.08.073.

66. Tateno, F., Sakakibara, R., Kishi, M., Tsuyusaki, Y., Furukawa, R., Yoshimatsu, Y., and Suzuki, Y. (2012). Brainstem Stroke and Increased Anal Tone. Low Urin Tract Symptoms *4*, 161-163. 10.1111/j.1757-5672.2012.00143.x.

67. Trunnell, E.R., Baines, J., Farghali, S., Jackson, T., Jayne, K., Smith, R., and Stibbe, T. (2024). The need for guidance in antidepressant drug development: Revisiting the role of the forced swim test and tail suspension test. Regulatory Toxicology and Pharmacology *151*, 105666. https://doi.org/10.1016/j.yrtph.2024.105666.

68. Nestler, E.J., and Hyman, S.E. (2010). Animal models of neuropsychiatric disorders. Nat Neurosci *13*, 1161-1169. 10.1038/nn.2647.

69. Hassabis, D., Kumaran, D., Summerfield, C., and Botvinick, M. (2017). Neuroscience-Inspired Artificial Intelligence. Neuron *95*, 245-258. 10.1016/j.neuron.2017.06.011.

70. Park, S., and Whang, M. (2022). Empathy in Human-Robot Interaction: Designing for Social Robots. Int J Environ Res Public Health *19*. 10.3390/ijerph19031889.

71. Kim, K.J., Ramiro Diaz, J., Iddings, J.A., and Filosa, J.A. (2016).

Vasculo-Neuronal Coupling: Retrograde Vascular Communication to Brain Neurons. J Neurosci *36*, 12624-12639. 10.1523/jneurosci.1300-16.2016.

72. Moore, C.I., and Cao, R. (2008). The hemo-neural hypothesis: on the role of blood flow in information processing. J Neurophysiol *99*, 2035-2047. 10.1152/jn.01366.2006.

73. Jammal Salameh, L., Bitzenhofer, S.H., Hanganu-Opatz, I.L., Dutschmann, M., and Egger, V. (2024). Blood pressure pulsations modulate central neuronal activity via mechanosensitive ion channels. Science *383*, eadk8511. 10.1126/science.adk8511.

74. Attwell, D., Buchan, A.M., Charpak, S., Lauritzen, M., Macvicar, B.A., and Newman, E.A. (2010). Glial and neuronal control of brain blood flow. Nature *468*, 232-243. 10.1038/nature09613.

75. Zeilhofer, H.U., Studler, B., Arabadzisz, D., Schweizer, C., Ahmadi, S., Layh, B., Bösl, M.R., and Fritschy, J.M. (2005). Glycinergic neurons expressing enhanced green fluorescent protein in bacterial artificial chromosome transgenic mice. J Comp Neurol *482*, 123-141. 10.1002/cne.20349.

76. Rampon, C., Luppi, P.H., Fort, P., Peyron, C., and Jouvet, M. (1996). Distribution of glycine-immunoreactive cell bodies and fibers in the rat brain. Neuroscience *75*, 737-755. 10.1016/0306-4522(96)00278-3.

77. Seo, J.S., Park, J.Y., Choi, J., Kim, T.K., Shin, J.H., Lee, J.K., and Han,

P.L. (2012). NADPH oxidase mediates depressive behavior induced by chronic stress in mice. J Neurosci *32*, 9690-9699. 10.1523/JNEUROSCI.0794-12.2012.

78. Sturman, O., Germain, P.L., and Bohacek, J. (2018). Exploratory rearing: a context- and stress-sensitive behavior recorded in the open-field test. Stress *21*, 443-452. 10.1080/10253890.2018.1438405.

79. Oyarzabal, E.A., Hsu, L.M., Das, M., Chao, T.H., Zhou, J., Song, S., Zhang, W., Smith, K.G., Sciolino, N.R., Evsyukova, I.Y., et al. (2022). Chemogenetic stimulation of tonic locus coeruleus activity strengthens the default mode network. Sci Adv *8*, eabm9898. 10.1126/sciadv.abm9898.

80. Yu, X.D., Zhu, Y., Sun, Q.X., Deng, F., Wan, J., Zheng, D., Gong, W., Xie, S.Z., Shen, C.J., Fu, J.Y., et al. (2022). Distinct serotonergic pathways to the amygdala underlie separate behavioral features of anxiety. Nat Neurosci *25*, 1651-1663. 10.1038/s41593-022-01200-8.

81. Jin, Y., Shi, P., Wang, Y., Li, J., Zhang, J., Zhao, X., Ge, Y., Huang, Y., Guo, M., Wang, F., et al. (2022). Precise control of embolic stroke with magnetized red blood cells in mice. Commun Biol *5*, 136. 10.1038/s42003-022-03082-9.

82. Li, J., Zhang, Y., Zhang, D., Wang, W., Xie, H., Ruan, J., Jin, Y., Li, T., Li, X., Zhao, B., et al. (2024). Ca(2+) oscillation in vascular smooth muscle cells control myogenic spontaneous vasomotion and counteract

post-ischemic no-reflow. Commun Biol *7*, 332. 10.1038/s42003-024-06010-1.

83. Li, W., Prakash, R., Chawla, D., Du, W., Didion, S.P., Filosa, J.A., Zhang, Q., Brann, D.W., Lima, V.V., Tostes, R.C., and Ergul, A. (2013). Early effects of high-fat diet on neurovascular function and focal ischemic brain injury. Am J Physiol Regul Integr Comp Physiol *304*, R1001-1008. 10.1152/ajpregu.00523.2012.

84. Hou, W., Yao, J., Liu, J., Lin, X., Wei, J., Yin, X., Huang, H., Chen, X., Yang, G.Y., and He, X. (2023). USP14 inhibition promotes recovery by protecting BBB integrity and attenuating neuroinflammation in MCAO mice. CNS Neurosci Ther *29*, 3612-3623. 10.1111/cns.14292.

85. Khalil, V., Faress, I., Mermet-Joret, N., Kerwin, P., Yonehara, K., and Nabavi, S. (2023). Subcortico-amygdala pathway processes innate and learned threats. Elife *12*. 10.7554/eLife.85459.

86. Arakawa, H., Arakawa, K., Blanchard, D.C., and Blanchard, R.J. (2007). Scent marking behavior in male C57BL/6J mice: sexual and developmental determination. Behav Brain Res *182*, 73-79. 10.1016/j.bbr.2007.05.007.

87. Arakawa, H., Arakawa, K., Blanchard, D.C., and Blanchard, R.J. (2008). A new test paradigm for social recognition evidenced by urinary scent marking behavior in C57BL/6J mice. Behav Brain Res *190*, 97-104. 10.1016/j.bbr.2008.02.009.

88. Borelli, K.G., Blanchard, D.C., Javier, L.K., Defensor, E.B., Brandao, M.L., and Blanchard, R.J. (2009). Neural correlates of scent marking behavior in C57BL/6J mice: detection and recognition of a social stimulus. Neuroscience *162*, 914-923. 10.1016/j.neuroscience.2009.05.047.

89. McQuaid, R.J., Audet, M.C., and Anisman, H. (2012). Environmental enrichment in male CD-1 mice promotes aggressive behaviors and elevated corticosterone and brain norepinephrine activity in response to a mild stressor. Stress *15*, 354-360. 10.3109/10253890.2011.623249.

90. Liu, J., Li, D., Huang, J., Cao, J., Cai, G., Guo, Y., Wang, G., Zhao, S., Wang, X., and Wu, S. (2022). Glutamatergic Neurons in the Amygdala Are Involved in Paclitaxel-Induced Pain and Anxiety. Front Psychiatry *13*, 869544. 10.3389/fpsyt.2022.869544.

91. Warden, M.R., Selimbeyoglu, A., Mirzabekov, J.J., Lo, M., Thompson, K.R., Kim, S.Y., Adhikari, A., Tye, K.M., Frank, L.M., and Deisseroth, K. (2012). A prefrontal cortex-brainstem neuronal projection that controls response to behavioural challenge. Nature *492*, 428-432. 10.1038/nature11617.

Figure 1

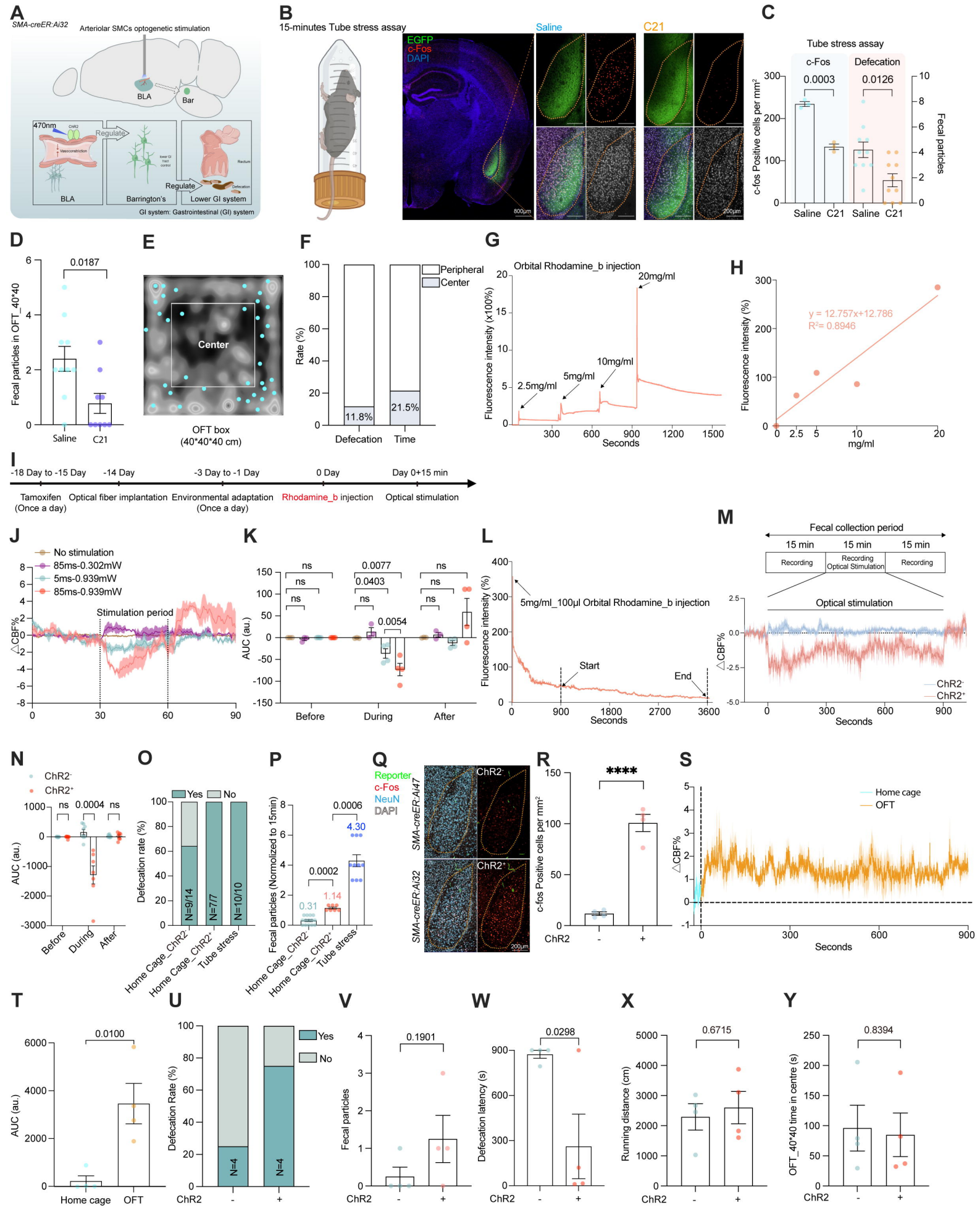
A
SMA-creER:Ai32
Arteriolar SMCs optogenetic stimulation
BLA
Bar
470nm
Regulate
Vasoconstriction
Rectum
Regulate
Defecation
BLA
Barrington's
Lower GI system
GI system: Gastrointestinal (GI) system
B
15-minutes Tube stress assay
Saline
C21
EGFP
c-Fos
DAPI
800μm
200μm
C
Tube stress assay
c-Fos
Defecation
0.0003
0.0126
c-fos Positive cells per mm²
Fecal particles
Saline
C21
Saline
C21
D
0.0187
Fecal particles in OFT_40*40
Saline
C21
E
Center
OFT box
(40*40*40 cm)
F
Peripheral
Center
Rate (%)
11.8%
21.5%
Defecation
Time
G
Orbital Rhodamine_b injection
20mg/ml
10mg/ml
5mg/ml
2.5mg/ml
Fluorescence intensity (x100%)
Seconds
H
y = 12.757x+12.786
R²= 0.8946
Fluorescence intensity (%)
mg/ml
I
-18 Day to -15 Day
-14 Day
-3 Day to -1 Day
0 Day
Day 0+15 min
Tamoxifen
(Once a day)
Optical fiber implantation
Environmental adaptation
(Once a day)
Rhodamine_b injection
Optical stimulation
J
No stimulation
85ms-0.302mW
5ms-0.939mW
85ms-0.939mW
Stimulation period
△CBF%
K
ns
0.0077
0.0403
0.0054
AUC (au.)
Before
During
After
L
5mg/ml_100μl Orbital Rhodamine_b injection
Start
End
Fluorescence intensity (%)
Seconds
M
Fecal collection period
15 min
15 min
15 min
Recording
Recording
Optical Stimulation
Recording
Optical stimulation
△CBF%
ChR2⁻
ChR2⁺
Seconds
N
ChR2⁻
ChR2⁺
ns
0.0004
ns
AUC (au.)
Before
During
After
O
Yes
No
Defecation rate (%)
N=9/14
N=7/7
N=10/10
Home Cage_ChR2⁻
Home Cage_ChR2⁺
Tube stress
P
0.0006
4.30
0.0002
1.14
0.31
Fecal particles (Normolized to 15min)
Home Cage_ChR2⁻
Home Cage_ChR2⁺
Tube stress
Q
Reporter
c-Fos
NeuN
DAPI
SMA-creER:Ai47
SMA-creER:Ai32
ChR2⁻
ChR2⁺
200μm
R
****
c-fos Positive cells per mm²
ChR2
-
+
S
Home cage
OFT
△CBF%
Seconds
T
0.0100
AUC (au.)
Home cage
OFT
U
Yes
No
Defecation Rate (%)
N=4
N=4
ChR2
-
+
V
0.1901
Fecal particles
ChR2
-
+
W
0.0298
Defecation latency (s)
ChR2
-
+
X
0.6715
Running distance (cm)
ChR2
-
+
Y
0.8394
OFT_40*40 time in centre (s)
ChR2
-
+

Figure 2

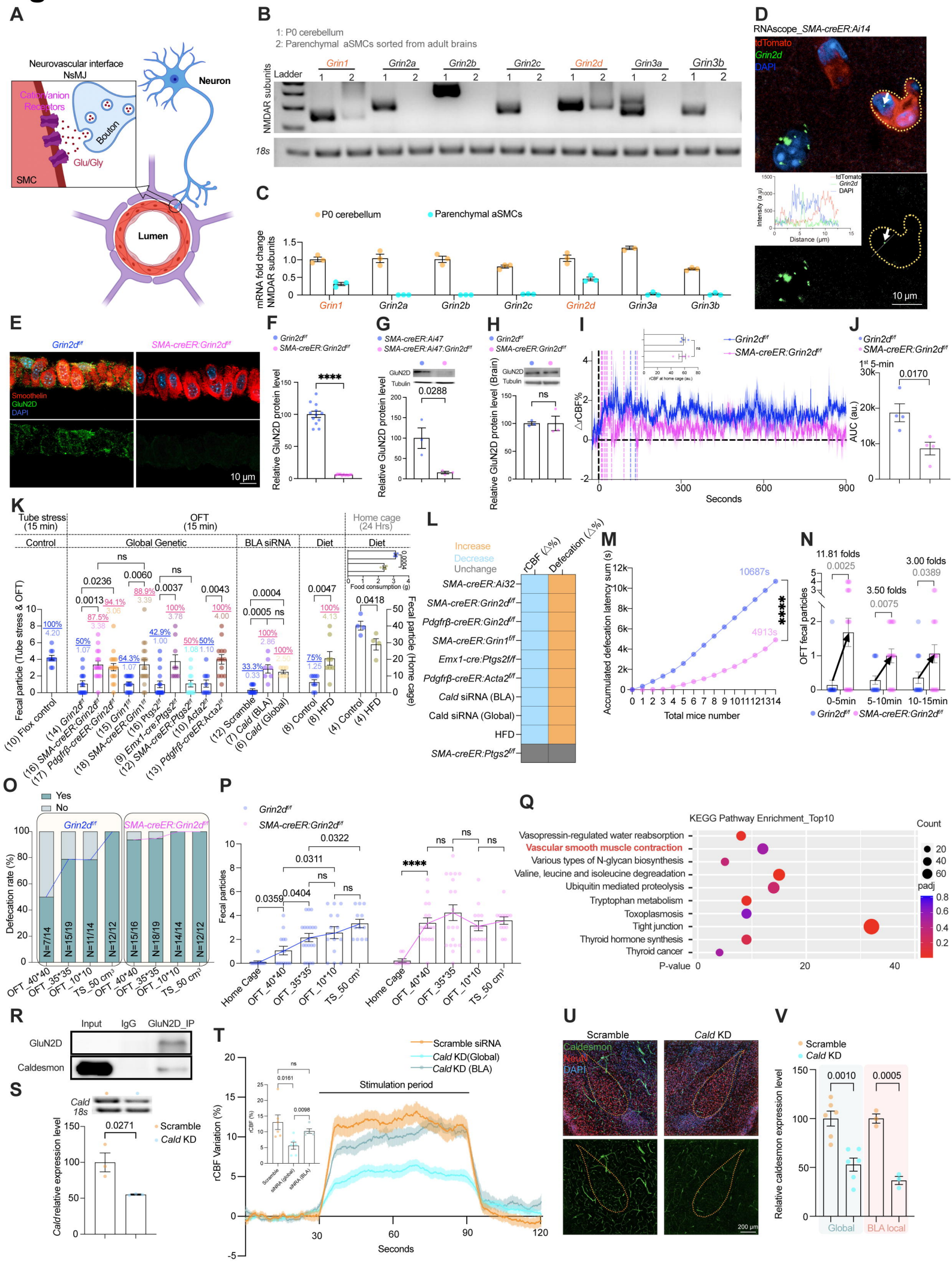
A
Neurovascular interface
NsMJ
Neuron
Cation/anion Receptors
Bouton
Glu/Gly
SMC
Lumen
B
1: P0 cerebellum
2: Parenchymal aSMCs sorted from adult brains
Ladder
Grin1
Grin2a
Grin2b
Grin2c
Grin2d
Grin3a
Grin3b
NMDAR subunits
18s
C
P0 cerebellum
Parenchymal aSMCs
mRNA fold change NMDAR subunits
D
RNAscope_SMA-creER:Ai14
tdTomato
Grin2d
DAPI
Intensity (a.u)
Distance (μm)
10 μm
E
Grin2d f/f
SMA-creER:Grin2d f/f
Smoothelin
GluN2D
DAPI
10 μm
F
Relative GluN2D protein level
****
G
SMA-creER:Ai47
SMA-creER:Ai47:Grin2d f/f
GluN2D
Tubulin
0.0288
H
Relative GluN2D protein level (Brain)
ns
I
△rCBF%
Seconds
rCBF at home cage (au.)
J
1st 5-min
AUC (au.)
0.0170
K
Tube stress (15 min)
OFT (15 min)
Home cage (24 Hrs)
Control
Global Genetic
BLA siRNA
Diet
Food consumption (g)
Fecal particle (Tube stress & OFT)
Fecal particle (Home cage)
(10) Flox control
(14) Grin2d f/f
(16) SMA-creER:Grin2d f/f
(17) Pdgfrβ-creER:Grin2d f/f
(15) Grin1 f/f
(18) SMA-creER:Grin1 f/f
(16) Ptgs2 f/f
(9) Emx1-cre:Ptgs2 f/f
(12) SMA-creER:Ptgs2 f/f
(10) Acta2 f/f
(13) Pdgfrβ-creER:Acta2 f/f
(12) Scramble
(7) Cald (BLA)
(6) Cald (Global)
(8) Control
(8) HFD
(4) Control
(4) HFD
L
Increase
Decrease
Unchange
rCBF (△%)
Defecation (△%)
SMA-creER:Ai32
SMA-creER:Grin2d f/f
Pdgfrβ-creER:Gin2d f/f
SMA-creER:Grin1 f/f
Emx1-cre:Ptgs2f/f
Pdgfrβ-creER:Acta2 f/f
Cald siRNA (BLA)
Cald siRNA (Global)
HFD
SMA-creER:Ptgs2 f/f
M
Accumulated defecation latency sum (s)
Total mice number
10687s
4913s
N
11.81 folds
3.00 folds
3.50 folds
OFT fecal particles
0-5min
5-10min
10-15min
O
Yes
No
Defecation rate (%)
N=7/14
N=15/19
N=11/14
N=12/12
N=15/16
N=18/19
N=14/14
N=12/12
OFT_40*40
OFT_35*35
OFT_10*10
TS_50 cm³
P
Fecal particles
Home Cage
Q
KEGG Pathway Enrichment_Top10
Count
padj
Vasopressin-regulated water reabsorption
Vascular smooth muscle contraction
Various types of N-glycan biosynthesis
Valine, leucine and isoleucine degradation
Ubiquitin mediated proteolysis
Tryptophan metabolism
Toxoplasmosis
Tight junction
Thyroid hormone synthesis
Thyroid cancer
P-value
R
Input
IgG
GluN2D_IP
GluN2D
Caldesmon
S
Cald
18s
Cald relative expression level
Scramble
Cald KD
T
Scramble siRNA
Cald KD(Global)
Cald KD (BLA)
Stimulation period
rCBF Variation (%)
Seconds
U
Scramble
Cald KD
Caldesmon
NeuN
DAPI
200 μm
V
Relative caldesmon expression level
Global
BLA local

Figure 3

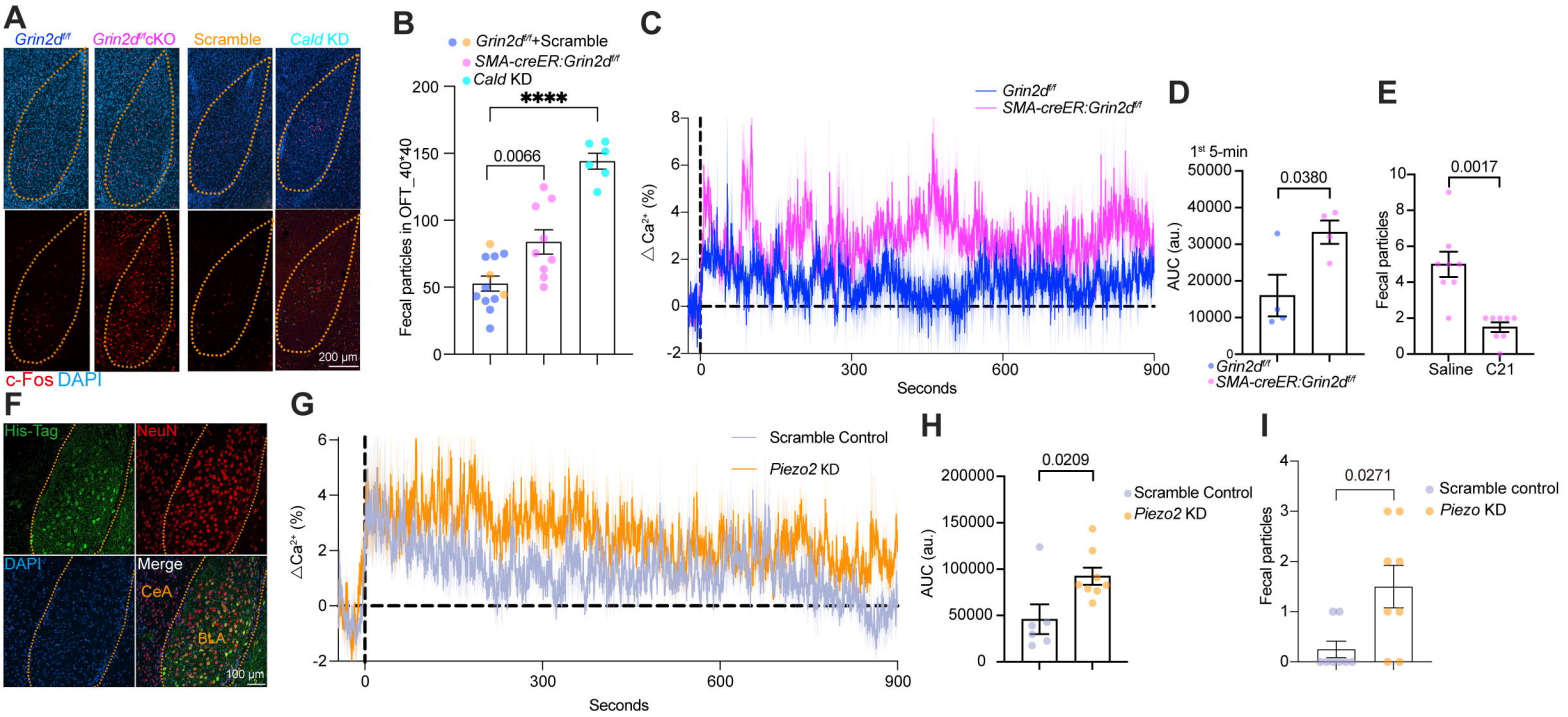
A
Grin2df/f
Grin2df/fcKO
Scramble
Cald KD
200 μm
c-Fos DAPI
B
Grin2df/f+Scramble
SMA-creER:Grin2df/f
Cald KD
Fecal particles in OFT_40*40
0.0066
****
C
Grin2df/f
SMA-creER:Grin2df/f
△Ca2+ (%)
Seconds
D
1st 5-min
AUC (au.)
0.0380
Grin2df/f
SMA-creER:Grin2df/f
E
Fecal particles
0.0017
Saline
C21
F
His-Tag
NeuN
DAPI
Merge
CeA
BLA
100 μm
G
Scramble Control
Piezo2 KD
△Ca2+ (%)
Seconds
H
AUC (au.)
0.0209
Scramble Control
Piezo2 KD
I
Fecal particles
0.0271
Scramble control
Piezo KD

Figure 4

Ruan et al.

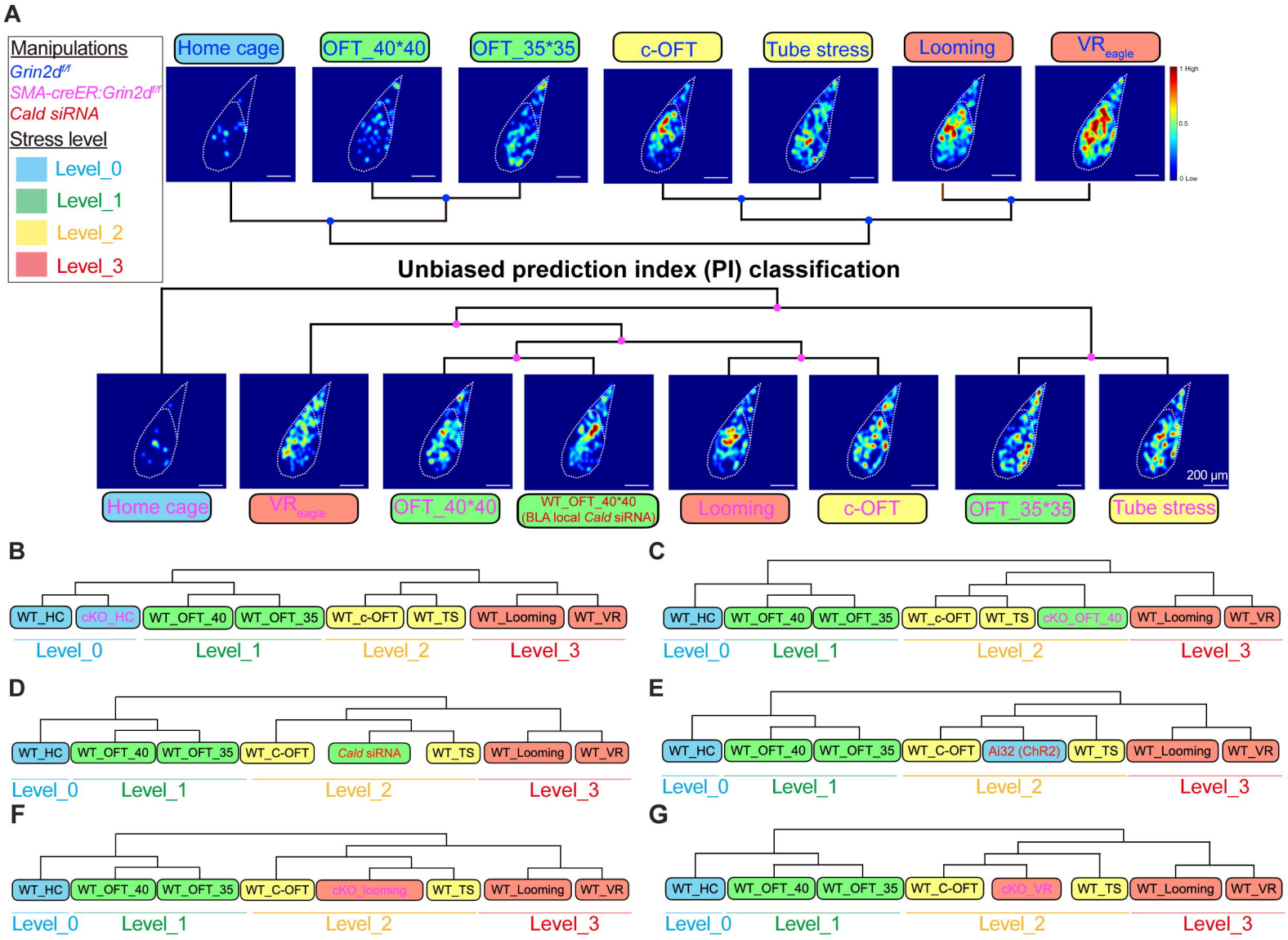

Figure 5

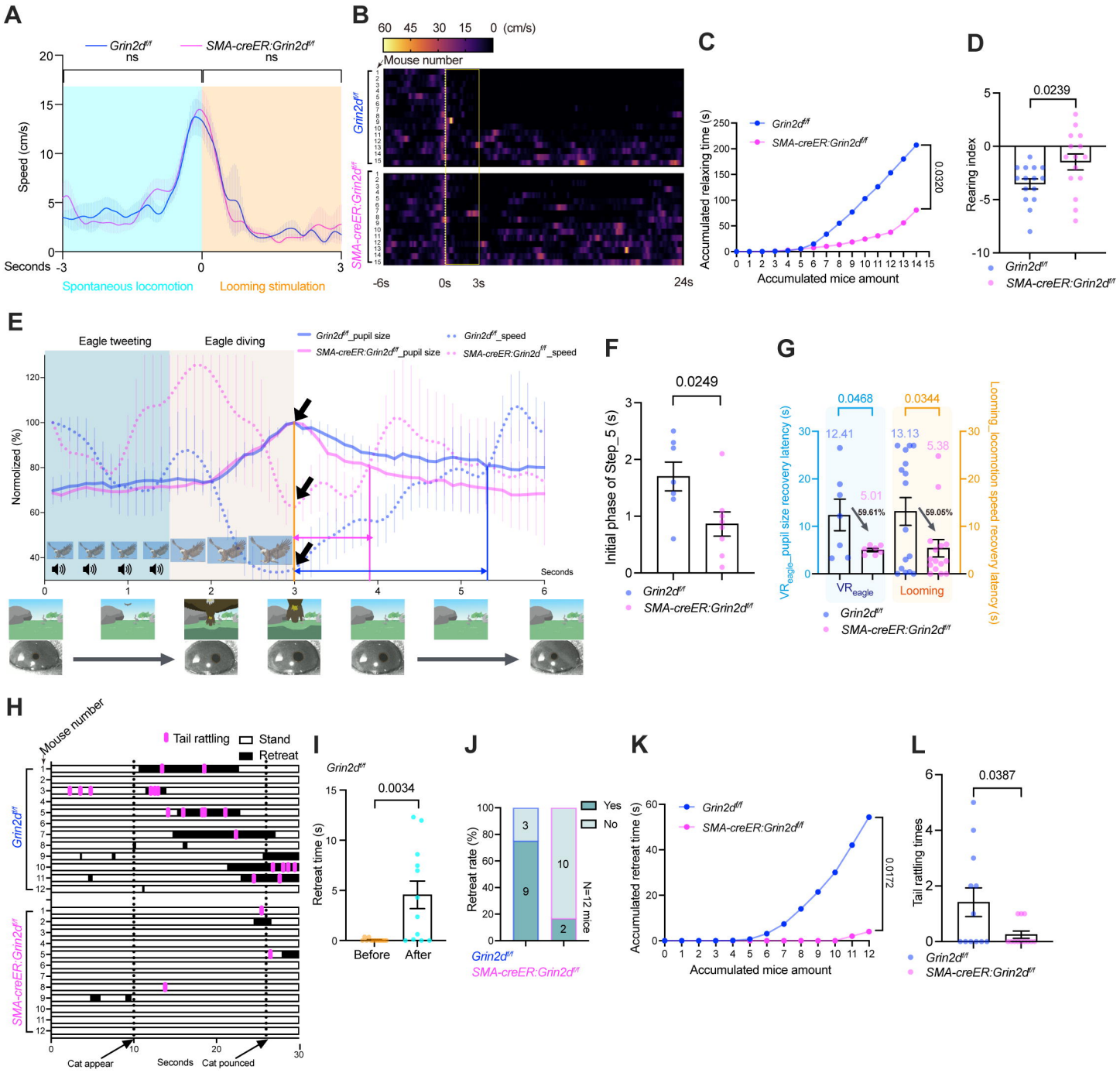
A
Grin2df/f
SMA-creER:Grin2df/f
ns
ns
Speed (cm/s)
Seconds -3
0
3
Spontaneous locomotion
Looming stimulation
B
60 45 30 15 0 (cm/s)
Mouse number
Grin2df/f
SMA-creER:Grin2df/f
-6s
0s
3s
24s
C
Accumulated relaxing time (s)
Grin2df/f
SMA-creER:Grin2df/f
0.0320
Accumulated mice amount
D
0.0239
Rearing index
Grin2df/f
SMA-creER:Grin2df/f
E
Eagle tweeting
Eagle diving
Grin2df/f_pupil size
SMA-creER:Grin2df/f_pupil size
Grin2df/f_speed
SMA-creER:Grin2df/f_speed
Normolized (%)
Seconds
F
0.0249
Initial phase of Step_5 (s)
Grin2df/f
SMA-creER:Grin2df/f
G
0.0468
0.0344
12.41
5.01
59.61%
13.13
5.38
59.05%
VReagle_pupil size recovery latency (s)
Looming_locomotion speed recovery latency (s)
VReagle
Looming
Grin2df/f
SMA-creER:Grin2df/f
H
Mouse number
Tail rattling
Stand
Retreat
Grin2df/f
SMA-creER:Grin2df/f
Cat appear
Seconds
Cat pounced
I
Grin2df/f
0.0034
Retreat time (s)
Before
After
J
Yes
No
Retreat rate (%)
3
9
10
2
N=12 mice
Grin2df/f
SMA-creER:Grin2df/f
K
Accumulated retreat time (s)
Grin2df/f
SMA-creER:Grin2df/f
0.0172
Accumulated mice amount
L
0.0387
Tail rattling times
Grin2df/f
SMA-creER:Grin2df/f

Figure 6

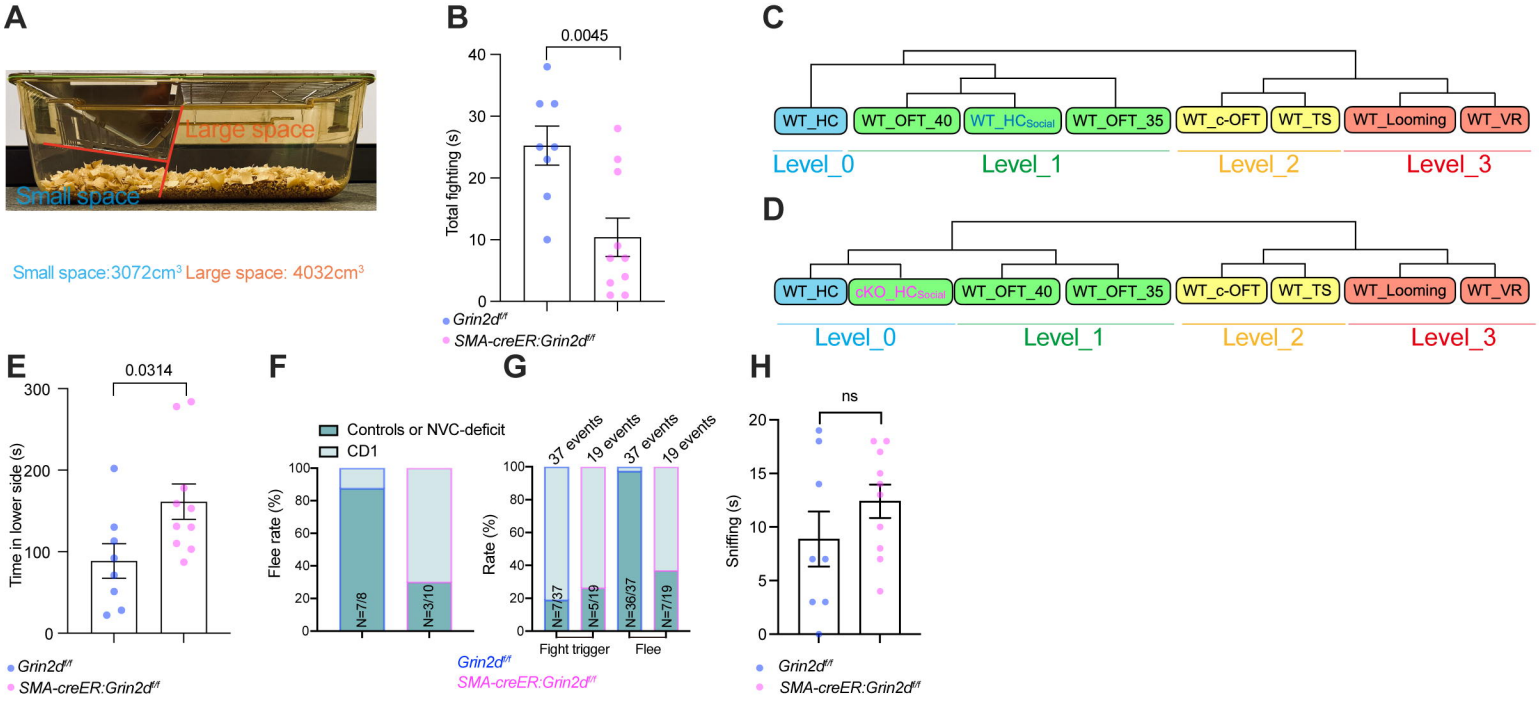
A
Large space
Small space
Small space:3072cm³ Large space: 4032cm³
B
0.0045
Total fighting (s)
Grin2df/f
SMA-creER:Grin2df/f
C
WT_HC
WT_OFT_40
WT_HCSocial
WT_OFT_35
WT_c-OFT
WT_TS
WT_Looming
WT_VR
Level_0
Level_1
Level_2
Level_3
D
WT_HC
cKO_HCSocial
WT_OFT_40
WT_OFT_35
WT_c-OFT
WT_TS
WT_Looming
WT_VR
Level_0
Level_1
Level_2
Level_3
E
0.0314
Time in lower side (s)
Grin2df/f
SMA-creER:Grin2df/f
F
Controls or NVC-deficit
CD1
Flee rate (%)
N=7/8
N=3/10
G
37 events
19 events
37 events
19 events
Rate (%)
N=7/37
N=5/19
N=36/37
N=7/19
Fight trigger
Flee
Grin2df/f
SMA-creER:Grin2df/f
H
ns
Sniffing (s)
Grin2df/f
SMA-creER:Grin2df/f

Figure 7
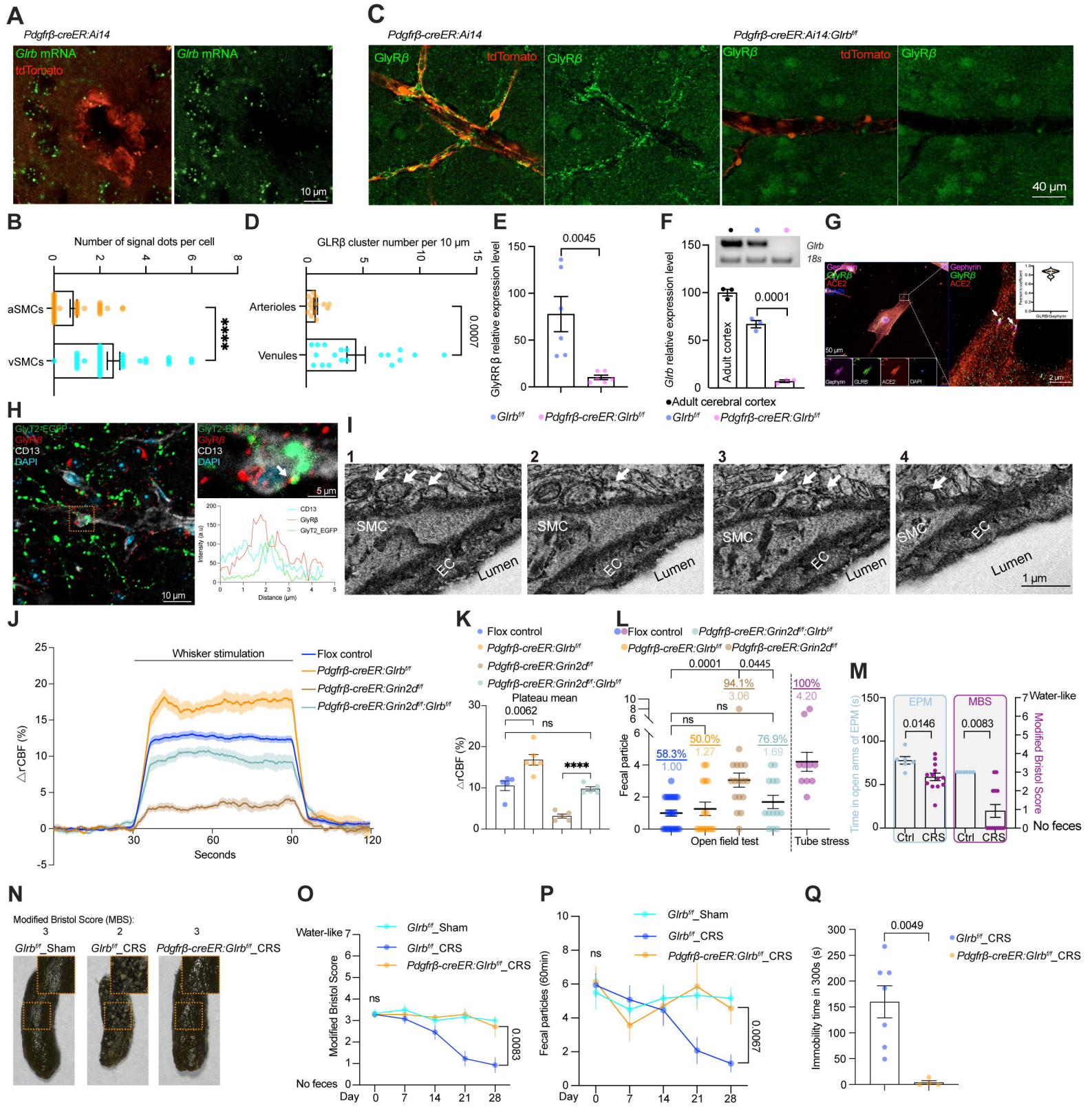
Ruan et al.